

Properties of the electron-hole liquid in Si: Zero stress to the high-stress limit

P. L. Gourley* and J. P. Wolfe

*Physics Department and Materials Research Laboratory,
University of Illinois at Urbana-Champaign,
Urbana, Illinois 61801*

(Received 30 March 1981; revised manuscript received 16 July 1981)

We have measured the properties of the electron-hole liquid (EHL) in Si as a function of stress from $\sigma=0$ to 163 kg/mm^2 which is well into the high-stress limit where the valence bands are decoupled. These measurements provide a useful test of many-body theories for EHL in crystals with a simple band structure. To produce these high stresses and to achieve some unique experimental advantages not realized in uniform-stress geometries, we have employed a well-characterized Hertzian stress geometry to strain ultrapure crystals of Si. This geometry creates an electronic potential minimum which confines both electrons and holes inside the crystal volume. At low temperature the e - h pairs spatially condense into a small volume (10^{-6} ml) of EHL at the bottom of the well. Because the liquid volume is small the EHL exists in a region of effectively uniform stress. This idea is confirmed by separate uniform-stress experiments which are included as a part of our study. We study the EHL properties by analyzing its photoluminescence with spectral, spatial, and time resolution under conditions in which stress, temperature, and photoexcitation level are varied over wide limits. In our spectral analysis, which incorporates stress-dependent band structure, we determine the Fermi energies and e - h pair density as it decreases from $3.5 \times 10^{18} \text{ cm}^{-3}$ at zero stress to $3.5 \times 10^{17} \text{ cm}^{-3}$ in the high-stress limit. Corresponding measurements of the intrinsic EHL time decay show that the lifetime increases from 0.14 to $3.0 \mu\text{s}$ over the same stress range. Combining the density and lifetime measurements, we are able to investigate the density dependence of the enhancement factor $g_{eh}(0)$ and the Auger process which dominates e - h recombination. We have measured a phase diagram for excitonic gas-EHL at high stress and find a critical point of $T_c \approx 20 \text{ K}$, $n_c \approx 2.5 \times 10^{17} \text{ cm}^{-3}$. In the high-stress limit the measured EHL binding energy is in the range $\phi = 1 - 1.4 \text{ meV}$. Additional spatial data reveal the presence of a repulsive force between droplets, possibly a "phonon wind," which inhibits large droplet formation. In general, the stress dependence of the ground-state properties shows trends which are in agreement with existing theories. However, some interesting discrepancies between our data and these theories are found.

I. INTRODUCTION

Photoexcitation of a pure semiconductor at low temperatures can produce a correlated two-component plasma known as the electron-hole liquid (EHL). This novel phase is an appealing subject from both theoretical and experimental points of view. It is a degenerate Fermi system whose properties can be reasonably well described by the Hartree-Fock calculation with correction for particle correlation. The basic many-body approach is to find the density n which minimizes the total pair energy $E_{\text{tot}}(n) = E_{\text{kin}} + E_{\text{ex}} + E_{\text{corr}}$, where the

terms represent kinetic, exchange, and correlation energies of the electrons and holes. The kinetic and exchange terms are well known. Several models have been suggested for the correlation energy and their relative merits await experimental tests. From the experimental side, the EHL may be easily produced and detected in the laboratory. The spectrum of photons emitted by recombining electrons and holes gives a one-to-one correspondence to the electronic states of the liquid. Thus the study of the EHL provides a very good test of advanced many-body theories.

Many theoretical and experimental studies have

been made of the equilibrium properties of the EHL in different crystals.^{1,2} Theoretical and experimental values for the equilibrium density and electron and hole Fermi energies agree to within 10–20% for the indirect-gap materials (Si, Ge, AgBr, and GaP) in which the EHL has been observed. Such close agreement has not yet been found for the direct-gap materials (e.g., GaAs and CdS), where the calculational and experimental difficulties are greater.

Effect of crystal stress on EHL

In his early predictions, Keldysh³ pointed out the great effect of band degeneracies on the stability of the electron-hole liquid. Thus the many-valley, indirect-gap materials such as Si and Ge

were expected (and found) to accommodate an electron-hole liquid which was highly bound with respect to free excitons (FE). Since the crystal strain removes these degeneracies, a stringent test for any theory of the EHL is provided by perturbing the crystal with an applied stress. The importance of crystal strain as a systematic test of the many-body theory was recognized in early studies of Si by Ashkinadze *et al.*⁴ and of Ge by Benoît à la Guillaume and Voos.⁵ They experimentally found lower density and reduced liquid binding energy in stressed crystals. Both results are consistent with a decrease in the density of electron and hole states due to the reduction in band degeneracy under crystal stress.

To illustrate these important ideas, the low-temperature luminescence spectrum of Si at several uniaxial, uniform stresses is shown in Fig. 1. At

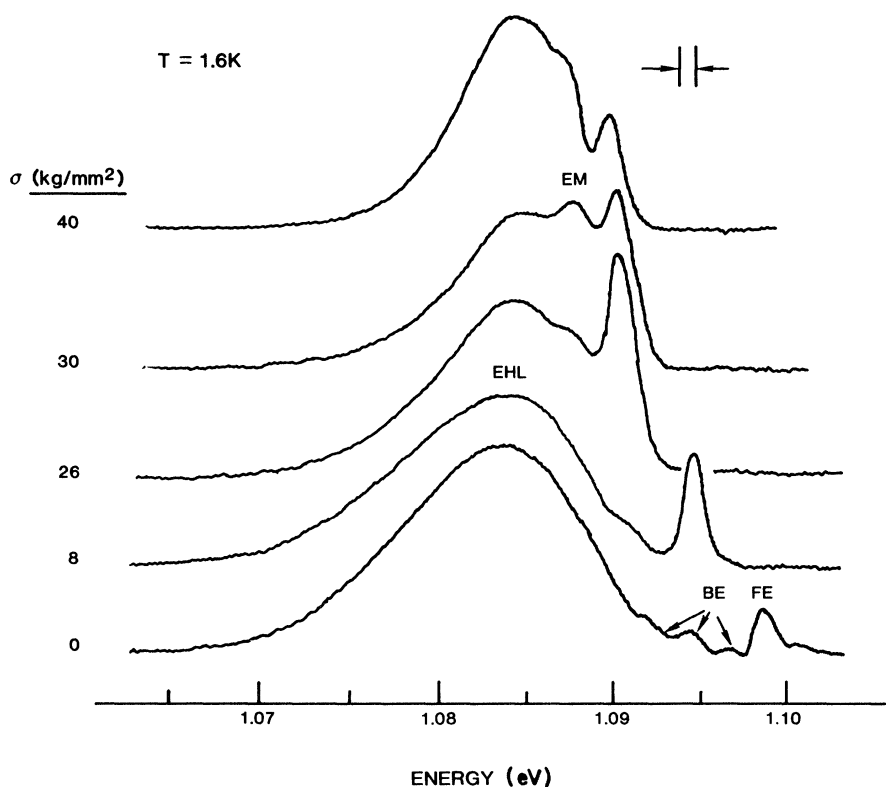


FIG. 1. TO-LO replica of the photoluminescence spectrum obtained at several uniform stresses by stressing a $1 \times 1 \times 10 \text{ mm}^3$ crystal of ultrapure Si between lead-tin pads. These spectra show the narrowing of the EHL and FE peak separation and the simultaneous enhancement of the gaseous phases, free excitons (rightmost peak, labeled FE at zero stress σ), and excitonic molecules (intermediate peak at high σ , labeled EM), with increasing stress. The energy scale applies to the bottom trace only. Subsequent traces have been shifted to align the EHL peaks for easy comparison. The absolute energy positions of the EHL and FE are given in Fig. 2. Except for the top trace where $P_{\text{ab}} = 100 \text{ mW}$, the absorbed laser power was $P_{\text{ab}} = 50 \text{ mW}$. The EHL line shape with uniform stress is difficult to analyze due to overlapping EM emission on the high-energy side. Bound excitons (BE) are evident at zero stress.

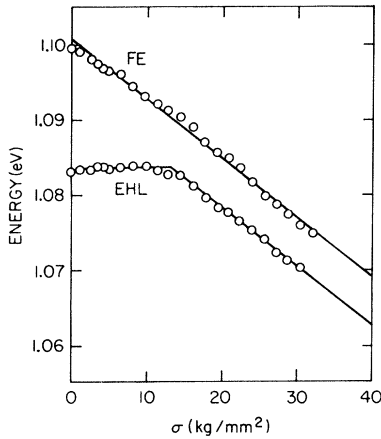


FIG. 2. Energy position of FE and EHL emission peaks versus $\langle 100 \rangle$ uniform stress. The EHL peak is unshifted until $\sigma \approx 13 \text{ kg/mm}^2$ marking the depopulation of the higher stress-split conduction bands.

zero stress the recombination at 1.083 eV from $e-h$ pairs in droplets of EHL is characterized by a very broad emission band with a width given by the EHL Fermi energy, $\epsilon_F = \epsilon_{Fe} + \epsilon_{Fh}$. The smaller peak at 1.098 eV is due to FE emission and has an intrinsic width of order kT , as expected for a Bose gas in the classical limit. The separation of these two emission lines gives the binding energy of the EHL. The peak positions of the EHL and free exciton are plotted versus $\langle 100 \rangle$ uniform stress in Fig. 2. The FE peak shifts to lower energy linearly

with stress, consistent with the known narrowing of the energy gap. The electron and hole states near the band edges are shown schematically in Fig. 3. At zero stress, six conduction-band ellipsoids are along $\langle 100 \rangle$ directions in wave-vector space, and the two warped valence bands have a maximum at $k=0$.

The energy of the EHL peak remains stationary at lower stresses. Thus the separation of the FE and EHL peaks decreases, as seen in Fig. 2. This indicates that the liquid $e-h$ binding energy relative to FE is decreasing. In short, the kinetic-energy term in the total pair energy contains $E_{Fe} = (\hbar^2 / 2m_{de})(3\pi n/d_e)^{2/3}$ which become relatively larger as the degeneracy d_e is lowered. The net result is to lower the equilibrium density n and reduce the binding energy ϕ . Correspondingly, the FE intensity (see Fig. 1) increases at the expense of the EHL intensity, indicating a higher evaporation rate of FE from the EHL. At a "critical" stress $\sigma_{ce} \approx 13 \text{ kg/mm}^2$ the EHL peak starts to shift, and it follows the FE energy thereafter. The critical stress marks the complete electron depopulation of the four upper conduction bands. The EHL linewidth, which is directly proportional to the Fermi energy, decreases significantly with strain. This indicates a large decrease in the equilibrium $e-h$ pair density n .

When the EHL is destabilized by crystal strain, the concentration of FE increases. Under these conditions substantial numbers of excitonic mole-

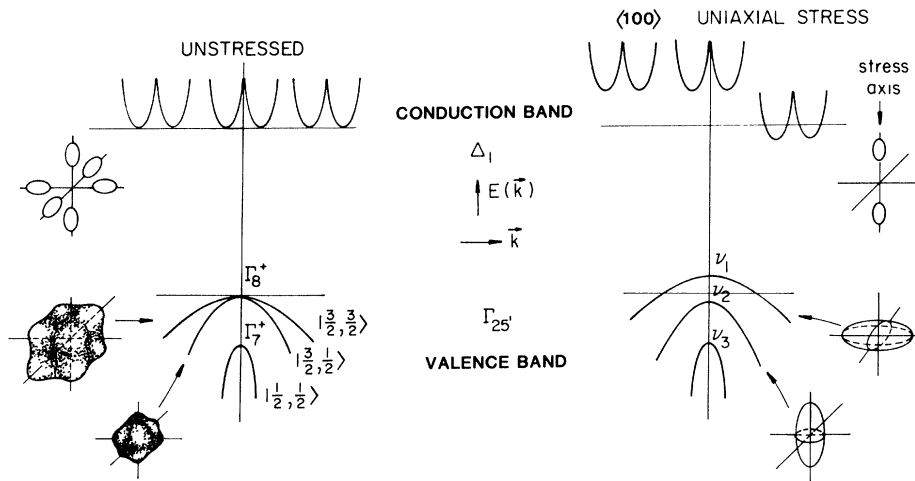


FIG. 3. Schematic diagram of Si-band extreme showing effects of $\langle 100 \rangle$ stress. The six conduction-band minima are represented by the three pairs of valleys. With stress the degeneracy is reduced from six to two. The coupled heavy and light valence bands exhibit cubically warped constant energy surfaces at zero stress. With stress these bands separate and have oblate and prolate energy surfaces at high stress.

cules (EM) can form.⁶⁻¹⁰ A separate emission peak due to EM occurs on the high-energy side of the EHL line, as seen in the upper traces of Fig. 1. With uniform strain it is difficult to determine the exact EHL line shape even at higher photoexcitation levels (top trace) because EM emission is present. The EM peak cannot be resolved and consequently broadens the EHL peak.

As one can see in Fig. 2, the EHL binding energy, which is represented by the FE-EHL spectral separation, is small and decreases slowly beyond the critical stress. In fact, early theoretical studies¹¹ suggested that the EHL might not be stable in the "high-stress limit." In the high-stress limit, only one parabolic valence band is occupied (cf. Fig. 3), and the theoretical description of the EHL is simpler. This limit is denoted by Si[2:1] where the numbers in brackets represent the conduction- and valence-band degeneracy, respectively. The high-stress limit for both Ge and Si is not attained until very large stresses $\sigma \simeq 100 \text{ kg/mm}^2$. Below this stress, the density of occupied valence-band states continues to change. This fact is shown explicitly in Fig. 4, which contains a plot of the valence-band density of states for several stresses.

The splitting of the two hole bands (Fig. 3) can be clearly seen here.

Previous experiments with stressed Si

The early stress work on Ge and Si demonstrated the fundamental importance of crystal strain on EHL. Subsequently, more detailed studies were carried out. However, in none of these was the high-stress limit $\sigma \simeq 100 \text{ kg/mm}^2$ actually reached. In all previous work on Ge, the highest stresses are about one order of magnitude lower than this. In Si they are lower by a factor of 2. In this paper we present a study of the EHL in Si from zero stress to $\sigma = 163 \text{ kg/mm}^2$. The maximum stress is 3 times higher than the previous work and is well into the desired high-stress limit. The high stresses were achieved with a Hertzian stress geometry which creates a potential-energy minimum in the bulk of the crystal to confine both electrons and holes.

The properties of Si stressed along $\langle 100 \rangle$, $\langle 110 \rangle$, and $\langle 111 \rangle$ directions have been studied by several workers. Kulakovskii *et al.*^{6,12} measured

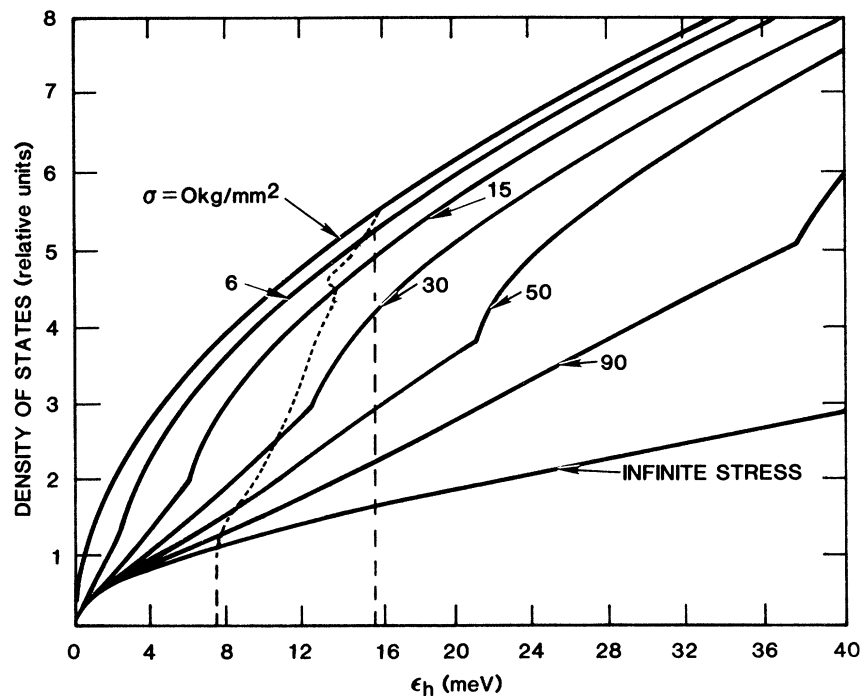


FIG. 4. Density of hole states (heavy line) at different stresses σ from zero stress to the high-stress limit. The zero energy is the bottom of the "lowest" hole band from which the hole energy ϵ_h is measured. The stress-split band can be followed by noting the position of the discontinuity which increases with stress. The dashed lines are explained later in the text.

the density, time decay, and binding energy at intermediate $\langle 100 \rangle$ stress, $\sigma = 48 \text{ kg/mm}^2$. They obtained $n = 4.8 \times 10^{17} \text{ cm}^{-3}$ in apparent agreement with the theory of Vashista *et al.*¹³ who calculated $n = 4.47 \times 10^{17} \text{ cm}^{-3}$. This close agreement now seems coincidental, since their analysis used the band structure of the high-stress limit. Wagner and Sauer¹⁴ found similar density changes for Si moderately stressed along $\langle 100 \rangle$. They obtained $n = 6 \times 10^{17} \text{ cm}^{-3}$ at $\sigma = 28 \text{ kg/mm}^2$, using the high-stress band structure. In both of these studies the stresses used to examine the EHL are well below the high-stress limit where the valence-band structure is simple. Not only is valence-band non-parabolicity present at lower stresses, but also these uniform-stress data contained a considerable broadening of the EHL emission by excitonic molecules. These two difficulties have been overcome in the experiments described below. A very recent study by Forchel *et al.*¹⁵ was made of the EHL critical temperature in Si stressed along the three principal crystal directions. However, the highest stress again falls short of the high-stress limit.

In summary, it must be concluded that until now no data has been reported for the EHL in the high-stress limit. Furthermore, no stress dependence of EHL properties in Si has been reported. We report a detailed stress dependence of the EHL properties from zero stress to 163 kg/mm^2 and

show that the liquid is stable in the high-stress limit. Also, we find that the $e-h$ pair density decreases 10 times from its zero-stress value while the lifetime increases 20 times.

In the following section we discuss the experimental methods used to obtain this data. Section III presents the piezospectroscopic data from which the density and Fermi energies are determined. The EHL decay kinetics and the enhancement factor are examined in Sec. IV. In Sec. V, measurements of the EHL at high temperature, the critical temperature, and binding energy are given. In Sec. VI we conclude the discussion of experimental results with a description of the spatial properties. A general discussion of these results concludes the paper in the final section.

II. EXPERIMENTAL TECHNIQUE

General discussion

The present work examines the spectral, spatial, and time-resolved photoluminescence of the EHL over a wide range of effectively uniform $\langle 100 \rangle$ stress. The experimental setup is displayed in Fig. 5. The crystal was mounted inside an optical cryostat and its temperature was regulated by liquid or gaseous helium. Modulated laser light was focused onto the crystal to generate electron-hole pairs.

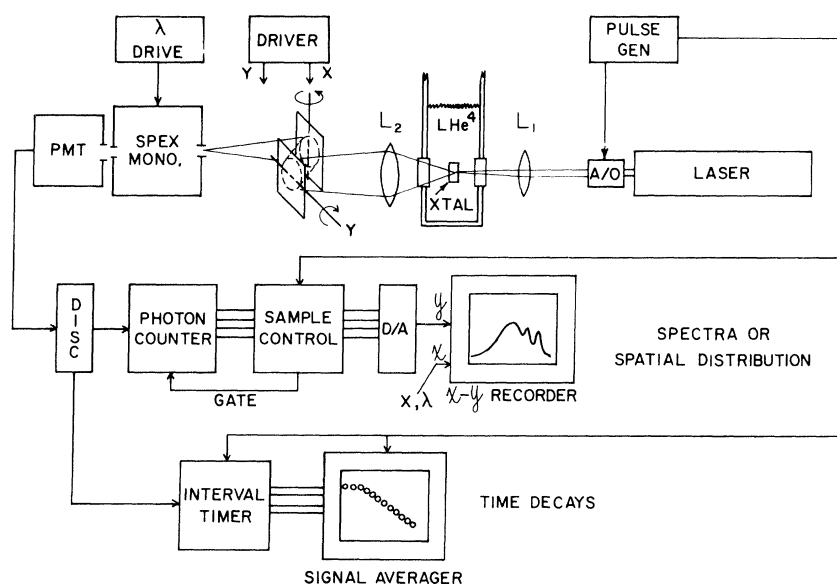


FIG. 5. General form of the experimental setup for recording photoluminescence with spectral, spatial, or temporal resolution.

The recombination radiation was collected with an $f/1.5$ lens, passed through a set of X-Y scanning mirrors, and focused onto the entrance slit of a spectrometer. At the exit slit was a Ge photodiode or a photomultiplier cathode. The resulting analog or digital signal was analyzed with subsequent electronics. Spectral resolution was obtained with a 0.5-m $f/6.8$ spectrometer. The grating had 1200 lines/mm and was blazed at $1\ \mu\text{m}$. With the slits typically set at $400\ \mu\text{m}$ the spectral resolution was 0.54 nm, or approximately 0.5 meV.

The deflection mirrors were used to position the crystal image at the spectrometer entrance aperture, which was either a vertical slit or a pinhole. In this way luminescence emanating from different regions in the crystal was selected. Spatial profiles of the luminescence were obtained by scanning the image across the entrance aperture. The spatial resolution was approximately $40\ \mu\text{m}$.

Luminescence time decays were measured with a digital interval timer in conjunction with a photomultiplier detector and a multichannel analyzer. Using an acousto-optic modulator, the light was turned on and off with ~ 100 ns rise and fall times. The interval timer measured the time between laser turn off and phototube pulse. The measurement was repeated with a high repetition rate and a histogram of the time intervals was collected in the analyzer. The steady-state luminescence intensity was attenuated, when necessary, to keep the average time between detected photons greater than 10 times the repetition period. Thus, a statistically valid representation of the luminescence was always obtained.

Two detector types were employed for sensing the 1.15–1.30 μm luminescence: a Varian VPM-164 photomultiplier tube and a Ge pin⁺ (p -type, “intrinsic”, n^+ -type) photodiode, each cooled to minimize thermal noise. The photodiode had a flat spectral response in the region of interest. It was used to study the EHL line shape. The photomultiplier had a response function which decreased rapidly over the above wavelength range. It was used in the digital technique of lifetime measurement described above.

Both surface- and volume-excitation sources were used to optically pump the crystal. The surface-excitation source was an Ar⁺ laser ($\lambda = 5145\ \text{\AA}$) with the absorption length $\sim 1\ \mu\text{m}$. Here the carriers were created at the surface, giving an overall generation rate in the strain potential well,

$$G_s = \frac{\epsilon_s(1-R_s)P}{h\nu_s}, \quad (1)$$

where P is the incident laser power, $h\nu_s$ the photon energy, and R_s is the reflectance of the crystal at $5145\ \text{\AA}$. The carriers quickly thermalize near the surface and a fraction ϵ_s are collected in the potential well which is about a millimeter inside the crystal.

In this work we have also employed a method for *directly* pumping the strain well. The “volume”-excitation source was a YAIG:Nd laser with $h\nu_v = 1.17$ eV, an energy slightly below the indirect absorption edge of unstressed Si at low T . Since strain lowers the band gap, absorption can be locally induced at the strain maximum. In this case the carriers are produced directly in the strain well in a nearly thermalized state. For small fractional absorption, this volume generation rate is

$$G_v = \frac{\epsilon_v P}{h\nu_v} \bar{\alpha} \Gamma, \quad (2)$$

where $\epsilon_v \simeq 1$ is the volume efficiency factor, and $\bar{\alpha}$ is the average absorption coefficient over the region of length Γ where absorption takes place. Since $h\nu_v$ is close to the band edge, $\bar{\alpha}$ is a very sensitive function of stress and temperature. A potentially important advantage of this direct-well-pumping technique is that the generation rate may be directly determined by measuring the laser light transmitted through the crystal, with and without stress or with the laser on and off the well.

The quantity ϵ_s/ϵ_v could be determined in a double laser experiment by separately adjusting the surface-excitation power to a value P_s which produced a luminescence intensity equal to that for volume excitation P_v with the YAIG:Nd laser focused on the well. Since negligible light is absorbed in low-stress regions of the crystal, the power absorbed by the volume excitation was measured directly from the difference δP in the transmitted power with the YAIG:Nd beam focused on and off the well. Then

$$\frac{\epsilon_s}{\epsilon_v} = \frac{h\nu_s}{h\nu_v} \frac{(1+R_v^2)}{(1-R_s)(1+R_v^2)} \frac{\delta P}{P_s}, \quad (3)$$

where R_v is the reflectance at $\lambda = 1.06\ \mu\text{m}$. This ratio was typically in the range 0.1–0.3. If ϵ_v is assumed equal to 1 (a reasonable assumption), the above measurement constitutes a measure of ϵ_s and consequently the number of e - h pairs produced in the well by surface excitation.

A reproducible, variable force for stressing the crystals in the optical cryostat was produced with the stressing apparatus shown in Fig. 6. By adjusting the micrometer, a variable spring force was

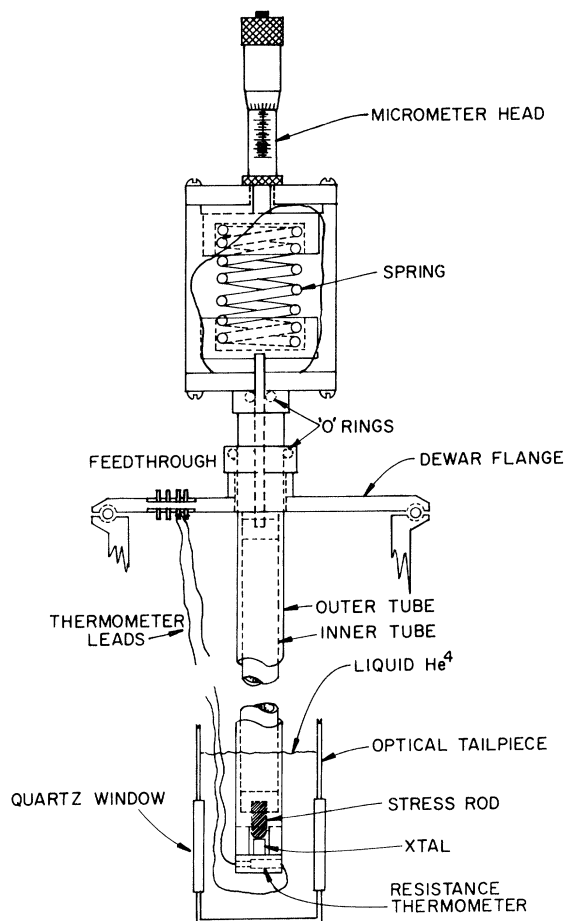


FIG. 6. Apparatus for performing variable-stress experiments at liquid-helium temperatures.

transmitted through a long steel tube to a small stress rod which contacted the crystal. The stress rods were small, cylindrical sections (~ 10 -mm long \times 3-mm diameter) cut from steel ball bearings with an electric discharge machine. The bearing surface was spherical with radius R . This radius and the applied force F were controllable parameters which characterized the stress distribution in the crystal.

The crystals were pressed into a bottom support disk machined from oxygen-free, high-conductivity copper. In the disk was embedded a small carbon resistor for temperature measurement. The temperature was controlled to within 0.1 K. The ultrapure Si crystals used in this work were Czochralsky grown and float-zone refined by Siemens and loaned to us by E. E. Haller of Lawrence Berkeley Laboratory. The crystals were oriented, cut to $4 \times 4 \times 1.8$ mm³, polished, and etched in a

solution of HNO₃ and HF. These high-resistivity crystals contained 2×10^{12} cm⁻³ boron impurities, which we estimated by the method of Tajima.¹⁶

Hertzian stress technique

An important technical aspect of these experiments, which differs considerably from previous experiments on EHL in stressed Si, was the technique of confining the EHL in a strain-induced electronic potential well. This potential well was produced in the crystal by a Hertzian stress distribution. Due in part to this strain-confinement method which is described below, we are able to make steady-state exciton measurements at very low excitation levels. The effective volume of photoexcited carriers was very small, permitting large average densities of excitons for relatively small excitation powers. Thus the problem of crystal heating frequently encountered for intense pulsed-laser excitation was avoided. In spite of the nonuniform method of applying stress, the electron-hole liquid was observed to occupy only a small region in the center of the strain well where the stress variation was negligible. Consequently, the liquid line shape was independent of excitation level over many orders of magnitude, despite an observed volume change in the liquid. This experiment indicated the absence of inhomogeneous linewidth broadening due to strain inhomogeneities. Indeed, all of the linewidths we measured were equal to or narrower than those previously obtained in uniform-stress experiments. Also, the Hertz stress method proved to be a much "gentler" means of stressing the crystals, since the stress rod does not contact the crystal near an edge, where fractures are most likely to occur. This explains why stresses up to 163 kg/mm² could be attained.

The Hertzian stressing method was first employed by the Berkeley group¹⁷⁻²³ to study large single EHL drops in Ge. In those experiments the Ge crystals were stressed by rounded nylon plungers. A detailed numerical study of the nylon and Ge stress distribution was carried out by Markiewicz *et al.*²⁴ The nylon stress rods had the advantage of forming a soft interface to the crystal, but the disadvantage was that only relatively low stresses could be applied without plastically deforming the stresser. More importantly, the stress could not be removed and reapplied at low temperatures with reproducible results, due to the hardened nature of the plastic at low temperatures. In

our initial studies on Si, we had no success with plastic stressers, apparently because of the higher stresses required to strain-confine EHL in Si. A systematic study of metal stressers was made which eventually allowed us a much more reproducible, variable strain than in the previous Ge experiments. Also, an order of magnitude was gained in the maximum stress attainable. In the present work a carefully flattened surface of a Si crystal was stressed with a spherical surface of hardened steel. In contrast to the nylon stresser, this combination retained the essential features of the Hertz contact stress.

The ‘‘Hertzian contact problem’’ or the ‘‘Hertzian stress distribution’’ refers to the solution of a problem originally solved 100 years ago by Hertz.²⁵ A particular geometry for this contact stress, used in our experiments, is shown in Fig. 7. At zero force F the spherical surface of the steel stress rod and the flat polished surface of the Si crystal touch at only a point. As force is applied the contact becomes a surface of increasing area due to the elasticity of the two media. This results in a hemispherical pressure distributed over the area, which in turn creates internal stresses in the medium below. The principal stresses σ_r and σ_z are analyzed in Ref. 26 as a function of depth into the body. These functions are plotted in Fig. 8 along with the shear stress $\tau = \sigma_z - \sigma_r$, which is responsible for lifting the electron and hole band degeneracy in a semiconductor. (In the experimental results described later, the magnitude of the shear stress

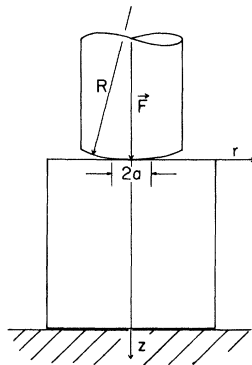


FIG. 7. Experimental stressing geometry for producing the Hertzian distribution. The Si crystal was $4 \times 4 \times 1.8\text{-mm}^3$ rectangular parallelepiped with all faces (100). The stresser, a cylindrical section cut from a ball bearing with radius R , is pushed against the crystal with force F . In the analysis, the contact surface is approximated by a circle of radius a .

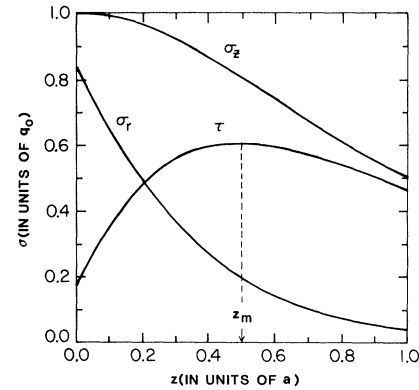


FIG. 8. The principal (normalized) stresses σ_r and σ_z and normalized shear stress $\tau = \sigma_z - \sigma_r$ versus reduced z coordinate in units of a . The shear stress maximum occurs at z_m .

maximum is denoted with σ .) As seen in this figure τ passes through a maximum inside the crystal. This shear stress maximum produces a potential-energy minimum for both electrons and holes. The stress maximum is characterized by three important parameters: the position of the maximum shear z_m , the value of the maximum shear τ_m , and the curvature $\alpha' = \partial^2 \tau / \partial z^2$. It is the ability to accurately control these three parameters that led to the success of the present experiments. In an analysis too lengthy to report here, we found that these parameters depend on the external variables F and R in the following way:

$$\tau_m \sim F^{1/3} R^{-2/3}, \quad (4)$$

$$\alpha' \sim F^{-1/3} R^{-4/3}, \quad (5)$$

$$z_m \sim F^{1/3} R^{1/3}. \quad (6)$$

To test these conclusions we measured the strain-well parameters for different values of F and R by examining the properties of the luminescence. The force was changed with the variable stressing apparatus previously described while the radius was changed by using stressers cut from ball bearings of different radii, $R = 6.1, 3.8, 1.9,$ and 0.95 cm. The depth z_m was directly measured from the location of the luminescence. The magnitude of τ_m was determined by comparing the shift in the energy of the FE and EHL luminescence peaks with those in Si crystals strained with a calibrated, uniform stress [see Figs. 9(a) and 9(b)]. The curvature α of the strain potential well was determined by measuring the spatial extent of the FE gas trapped in the well at higher temperatures [see Fig. 9(c)]

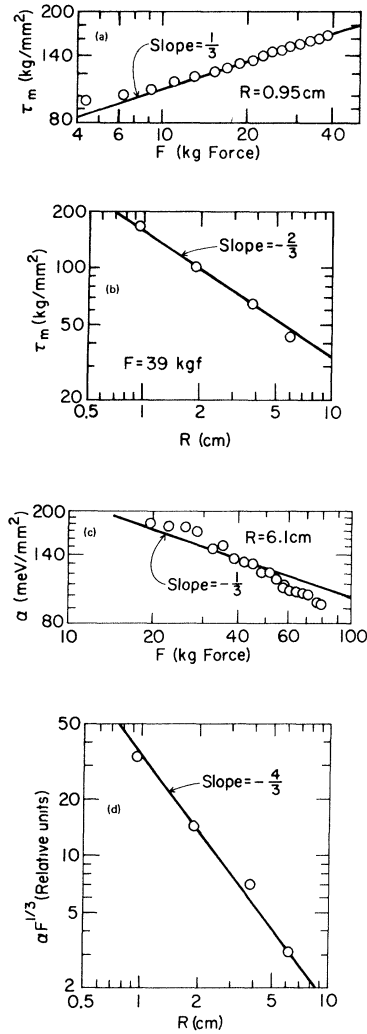


FIG. 9. (a) Shear stress maximum τ_m , determined by comparing the EHL luminescence position with the extrapolated values of the uniform strain data (Fig. 2), versus force applied to a stresser with a radius of 0.95 cm. (b) τ_m versus radius R of stresser at $F=39$ kg force. (c) Curvature α of the potential well versus applied force F . (d) The quantity $\alpha F^{1/3}$, proportional to α , versus the stresser contact surface radius R .

and 9(d)]. Specifically, the thermal-average potential energy of an exciton in a harmonic potential $V=\alpha r^2$ is given by

$$\langle \alpha r^2 \rangle = \frac{3}{2} kT. \quad (7)$$

The spatial distribution of particles in this well is Gaussian and the root-mean-square displacement $\langle r^2 \rangle$ is directly determined by measuring the full width at half maximum (FWHM) of the distribution.

Despite the simplistic approximations made in the Hertzian solution, this theory accurately accounts for the observed dependence [shown in Figs. 9(a)–9(d)] of the potential well parameters on the externally controlled variables F and R . By adjusting both F and R , the strain well could be constructed as needed for a particular kind of experiment. To produce a strain well deep into the sample requires a large force and large radius of curvature. A high-stress maximum will result with large force and small R . High curvature, to effect compression of the excitonic gas, requires small F and R .

An important result of this analysis is that we are able to demonstrate that the EHL line shape is not broadened by strain. Due to the relatively short EHL lifetime and the compression of the cloud of EHL droplets, the volume of liquid is confined to a very small region of negligible strain variation at the bottom of the well. This can be seen by comparing a typical EHL Fermi energy ϵ_F with the variation energy (per $e-h$ pair) over the occupied region of the well. For example, a 40 kg force applied with an $R=6.1$ cm stresser creates a well with curvature $\alpha=38$ meV/mm², a typical EHL spatial FWHM for this potential well is 100 μm so that the average strain energy $\langle \alpha r^2 \rangle = 0.36$ meV which is much less than $\epsilon_F = 10$ meV. A similar force applied with an $R=0.95$ cm stresser produces $\alpha=550$ meV/mm². However, in this steeper potential well, the FWHM is about 30 μm so that $\langle \alpha r^2 \rangle = 0.45$ meV, again much less than ϵ_F . Thus the EHL volume is effectively a region of uniform stress. As mentioned before, this is supported by the lack of any EHL line shape broadening over a wide range of excitation level. Moreover, the linewidth continuously narrows as a function of stress as we will demonstrate shortly. Only with exceptionally high excitation (absorbed power of 0.5 W) with the $R=0.95$ cm stresser, was a small 15% stress broadening present. It is probable that under these conditions the volume of EHL is approaching a large single drop.

III. SPECTROSCOPY OF EHL IN STRESSED Si

We measured the luminescence from EHL in the strain potential well at many closely spaced values of stress. Representative EHL luminescence line shapes at zero, intermediate, and high stress are shown in Fig. 10. In this figure the energy position of the peaks have been aligned for easy com-

parison of the line shapes. The spectral full width at half maximum (FWHM) decreases by more than a factor of 2 from zero to high stress. This indicates a greatly reduced density at high stress. The line shape asymmetry due to the low-energy tail is apparent at all stresses, but it is more pronounced in the high-stress line shape. The small peak at higher energy, present in both the zero- and intermediate-stress spectra, is emission from free excitons. The exciton peak is absent in the high-stress spectrum.

In Sec. VI we will present evidence that at the lower stresses the EHL exists as a cloud of small droplets immersed in excitonic gas. The high-stress spectrum, on the other hand, is more likely associated with a large contiguous volume of EHL. This is because the excitonic gas is highly compressed for large stresses. Another noteworthy feature in these spectra is the reduction of EHL binding energy with increasing stress. This is apparent from the decrease in the separation of the EHL and FE peaks as the stress increases.

Figure 11 gives the stress dependence of the EHL spectral FWHM from zero stress to $\sigma = 163 \text{ kg/mm}^2$. In order to completely span this extremely wide range of stresses, four different stressing conditions were used. The lowest stresses were obtained with a uniform stress configuration while

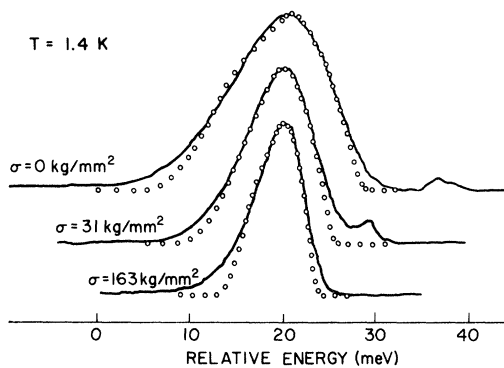


FIG. 10. Spectral line shape of the TO-LO replica for the EHL at zero stress and strain-confined EHL at intermediate and very high stress showing a twofold reduction in the spectral FWHM and thus a greatly reduced e - h pair density. The fit (open points), described in Appendix A, determines the density. The line shape at $\sigma \approx 163 \text{ kg/mm}^2$ corresponds to the first observation of an EHL in the high-stress limit. The horizontal scale indicates the relative energy, as the EHL peaks have been aligned for comparison. The EHL peak positions at $\sigma = 0, 31, \text{ and } 163 \text{ kg/mm}^2$ are 1.083, 1.068, and 0.967 eV, respectively.

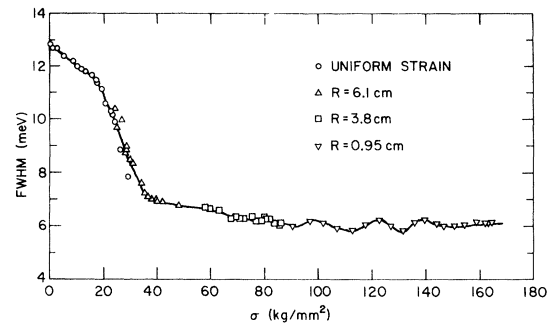


FIG. 11. Spectral FWHM (data points) of the EHL line shape versus $\langle 100 \rangle$ stress. To obtain data over a wide stress range, a uniform-stress geometry and a Hertzian stress geometry with several different values for R , the radius of the spherical contacting surface were employed.

three sequentially higher stress ranges were obtained with three different Hertzian stress configurations, each employing a different radius for the spherical stresser contact. The consistent overlap of these different runs indicated that the experimental curve was independent of the exact stressing condition. Furthermore, from $\sigma = 22$ – 24 kg/mm^2 the uniform-stress and Hertzian stress data show very close agreement, affirming the idea of effective uniform stress for EHL in the strain well. The linewidth slowly decreases between $\sigma = 0$ and 16 kg/mm^2 and then falls sharply until 36 kg/mm^2 . Here it abruptly levels off and then decreases slowly until 100 kg/mm^2 . Above $\sigma = 100 \text{ kg/mm}^2$, the infinite stress limit is reached and the linewidth does not change appreciably. However, some interesting oscillations, which we believe are above the uncertainty level, occur in the high-stress region.

The fitting functions (open points) in Fig. 10 are the usual convolution of the electron- and hole-energy distributions²⁷ modified to account for crystal stress. Such a fit at each stress determines the pair density and electron and hole Fermi energies. The theoretical line shape incorporates stress-dependent densities of states which account for degeneracy lifting and valence-band nonparabolicity (Fig. 4). The details of the line shape and the fitting procedure are described in Appendix A.

In the traces of Fig. 10 there is a discrepancy between the fitting functions and the experimental line shapes at the low-energy tail. The free-particle densities of electron and hole states, which are used in the fitting functions, cut off too sharply at low energy to account for the data. The extra low-energy tail observed in other EHL spectra has been

examined by several workers and attributed to lifetime broadening of energy levels.^{28,29} They modified the densities of states to account for the short time that a carrier occupies a given energy state. This produced a better fit corresponding to a small $\sim 6\%$ increase in the e - h pair density. We note, however, that this type of lifetime broadening should decrease with decreasing particle density. This is in apparent contradiction with our data, which displays a pronounced low-energy tail even at $10\times$ lower density. Because the correction is small, no such modification of the densities of states has been made in the present analysis of the line shape. Nevertheless, the discrepancy at low energy remains an important puzzle to understand.

In addition, there is a small discrepancy between theory and experiment at the high-energy side of the EHL luminescence peak. In a previous paper³⁰ we showed that this disparity could be removed by assuming a liquid temperature $T_{\text{EHL}} \simeq 5$ K higher than the lattice temperature. This suggested that the liquid simply did not have enough time to completely thermalize with the crystal lattice within its lifetime, or possibly that the lattice was warmed slightly by the photoexcitation, carrier thermalization, and recombination processes. These hypotheses do not seem to be supported by the fact the high-energy misfit is comparable for unstressed and stressed EHL, in which density and lifetime vary by over an order of magnitude (cf. below).

All data shown here are the TO-LO replicas of the EHL emission spectra. The fitting function, however, involves only a single replica. We have found that a double-replica fitting line shape, using the TO-LO energy separation and relative intensity given by Hammond *et al.*³¹ produces a negligible increase in the FWHM of the single replica. Furthermore, the ratio of the LO to TO intensity is apparently reduced with stress. This is indicated in the TO-LO spectra at very low excitation. The much weaker TA replica of the EHL had a spectral width that was approximately 8% narrower than that for the TO-LO replica. The difference cannot be satisfactorily accounted for with the overlapping TO-LO replicas and has been previously discussed.³²

The electron and hole Fermi energies determined in the fitting analysis are plotted as a function of stress in Fig. 12. Notice the transition behavior of the Fermi energies near $\sigma = 13$ kg/mm² where the conduction-band splitting (solid line labeled Δ_e) equals the electron Fermi energy ϵ_{F_e} . At this

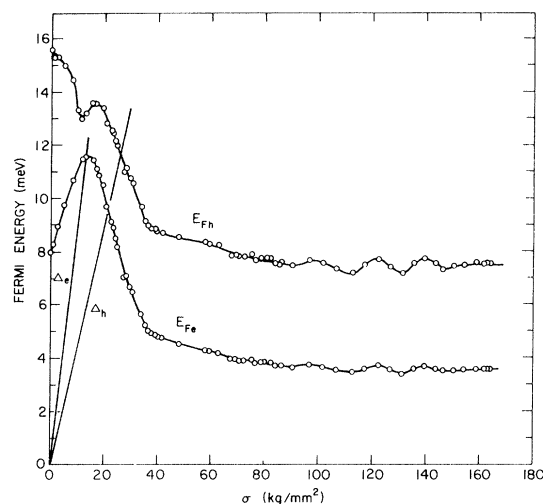


FIG. 12. Electron and hole Fermi energies, determined by fitting in EHL line shapes, versus $\langle 100 \rangle$ stress σ . The lines labeled Δ_e and Δ_h are the stress splittings of the conduction and valence bands, respectively.

stress the conduction-band degeneracy is lifted; the electron transfer from the four higher stress-split bands to the two lower bands is complete. The discontinuity occurs at approximately the same stress as the “critical” behavior seen in the stress-induced shift of the EHL peak in Fig. 2. The solid line labeled Δ_h determines a complete lifting of the valence-band degeneracy at $\sigma = 26$ kg/mm². However, at that stress there is no evidence of discontinuous changes in the Fermi energies. Instead, a knee is evident at $\sigma = 36$ kg/mm². In any event the depopulation of the “higher” (light-hole) stress-split valence band is not as dramatic as the conduction-band depopulation. This is because the light-hole contribution to the density of states is small, in contrast to the large density of higher, stress-split states in the conduction band. The changes in the Fermi energies above $\sigma \simeq 13$ kg/mm² are primarily due to the change in the heavy-hole density-of-states effective mass. This can be seen in Fig. 4, where the density of hole states decreases rapidly from $\sigma = 0$ to 50 kg/mm² and more slowly from 50 to 100 kg/mm². Beyond 100 kg/mm² the mass does not change appreciably and the Fermi energies are relatively constant. However, small oscillations in the Fermi energy are evident at higher stresses $\sigma = 100 - 150$ kg/mm². In Fig. 4 we have drawn the fine dashed line which indicates the filling level (Fermi energy from Fig. 12) of the hole density of states at each stress. By

observing the integrated area under the $\sigma=0$ and ∞ curves (the coarse dashed lines are the upper limits), one can visualize the large $10\times$ reduction in the density.

We can compare our measurements of the Fermi energies in the low-stress region to those recently predicted by Kirczenow and Singwi³³ by plotting them (in units of the simple exciton Rydberg $E_{x0}=12.85$ meV) versus Δ_h in Fig. 13. There are significant differences between their theory and our measurements. These are most evident in the intermediate-stress region, where the theoretical difficulties are largest. However, similar trends are observed.

The e - h pair density at each stress was determined, as detailed in Appendix A, from the knowledge of the Fermi energy and the density of states. The density plotted in Fig. 14 against σ , monotonically decreases with stress by a factor of 10. Like the plot of the Fermi energies, some features are evident near the stresses where depopulation occurs. The zero-stress density is 3.5×10^{18} cm^{-3} in close agreement with previous measurements.³¹ The high-stress value is 3.5×10^{17} cm^{-3} .

This value is significantly lower than measured densities reported by other authors^{12,14,15} to be in the high-stress limit. Those measurements, also shown in Fig. 14 (square data points), did not account for the valence-band nonparabolicity still present at intermediate stresses.

In order to compare our measured densities with theoretical results, we have plotted the experimental density (points) in the low-stress region as a function of Δ_h in Fig. 15. The solid lines are theoretical stress dependence of the density calculated by Kirczenow and Singwi.³³ As mentioned in the figure caption these two curves differ in the method of calculating the correlation energy. There is good agreement between the zero- and high-stress data and the curve labeled SPH (single particle hole). Although the theoretical and experimental values disagree in the intermediate-stress region, the same general trends are evident. Notably, there are sharp features at the critical stresses and the same initial turnover and gradual decrease to the high-stress limit. In the high-stress limit we have also indicated (arrow) the limiting value of density determined in the present experiments.

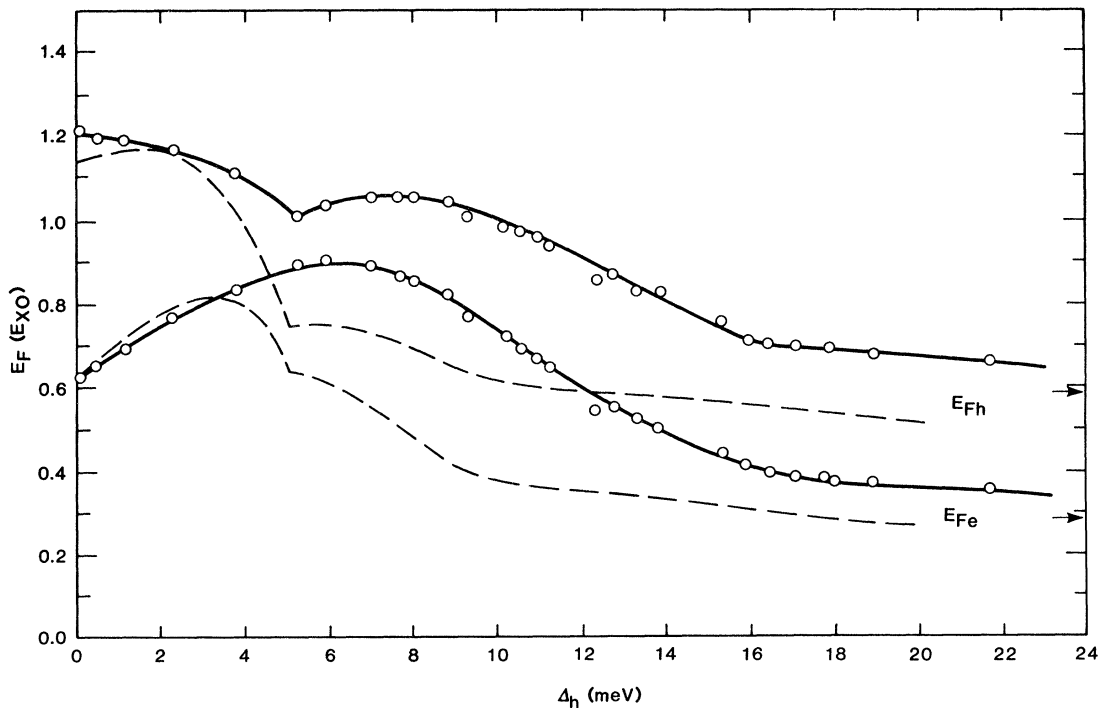


FIG. 13. Electron and hole Fermi energies, in units of the exciton Rydberg, versus valence-band splitting Δ_h . The open circles are low-stress data from Fig. 12 that have been replotted to compare with theoretical results (dashed lines) of Kirczenow and Singwi (Ref. 33). The arrows indicate the highest stress data corresponding to $\Delta_h = 73$ meV. The theory uses the single particle-hole (SPH) method to calculate the exchange energy.

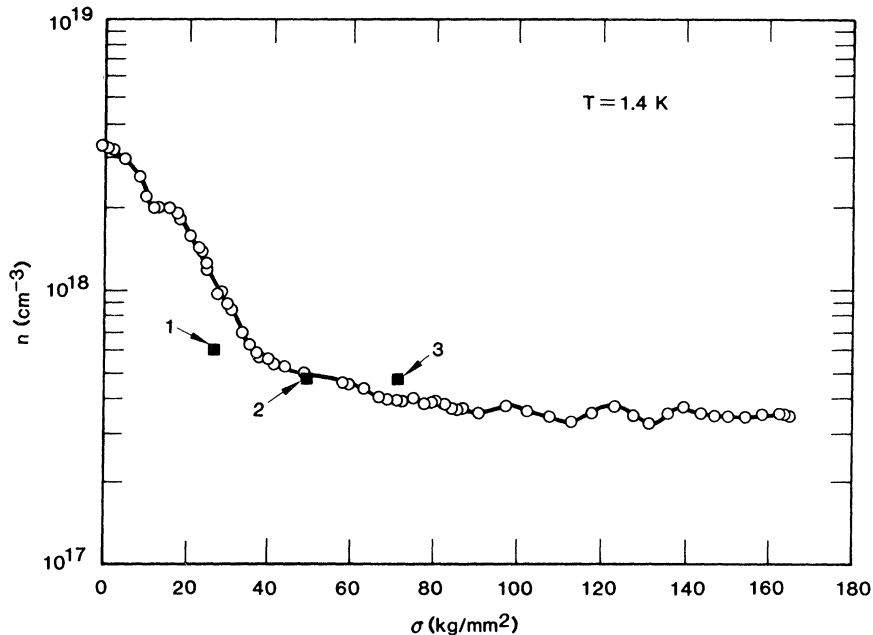


FIG. 14. The electron-hole pair density in the EHL versus $\langle 100 \rangle$ stress. The densities are determined with the Fermi energies of Fig. 12 in a procedure described in Appendix A. For comparison we include the data points (squares) of (1) Wagner and Sauer (Ref. 14), (2) Kulakovskii *et al.* (Ref. 12), and (3) Forchel *et al.* (Ref. 15).

Theoretical values for the density in the high-stress limit have been calculated by Vashista *et al.*¹³ and Kelso³⁴ who have used a fully self-consistent correlation energy. These values, as well as that calculated by Forchel *et al.*¹⁵ are about 30% larger than our experimental value.

IV. EHL LIFETIME AND THE ENHANCEMENT FACTOR

EHL decay kinetics

The recombination rate of electrons and holes within the EHL is strongly dependent upon its equilibrium properties. In this section we relate the EHL lifetime to the equilibrium density which changes by a factor of 10 with stress. The time decays of the EHL luminescence were measured over a range of stresses 0–170 kg/mm² using the timing technique described in the experimental section. Three of these time decays, at zero, intermediate, and high stress, are shown in Fig. 16. All of these decays are exponential and show a marked increase in the lifetime with increasing stress. The longer lifetimes are directly related to the decrease in e - h pair density examined in the preceding section. This type of stress-induced lifetime enhancement

was first reported for strain-confined EHL in Ge by Wolfe *et al.*¹⁸ The zero-stress lifetime in Si is 0.14 μ s, and is in good agreement with previous measurements.^{35–37} The high-stress lifetime of 3.0 μ s represents a 20-fold increase over the zero-stress value.

This high-stress lifetime is much longer than previous measurements made at intermediate stress by Kulakovskii *et al.*¹² Those time decays of the EHL for Si in a $\langle 100 \rangle$ uniform-stress geometry were distinctly nonexponential. The decay rate they measured increased with time and the $1/e$ time was about 0.2 μ s. The cause of the nonexponential decay was attributed to an enhanced FE evaporation from EHL, which occurs when the EHL binding energy is reduced under stress. Under such conditions the observed EHL decay rate increases with evaporation and is not representative of a volume decay rate. Therefore, the uniform-stress geometry did not permit a determination of the intrinsic EHL decay even at moderate stresses.

In the present experiments this difficulty was precluded by the strain gradient of the potential well, which inhibits FE boiloff. Under conditions where the excitons are confined, the time decays are exponential and do not depend on the pumping

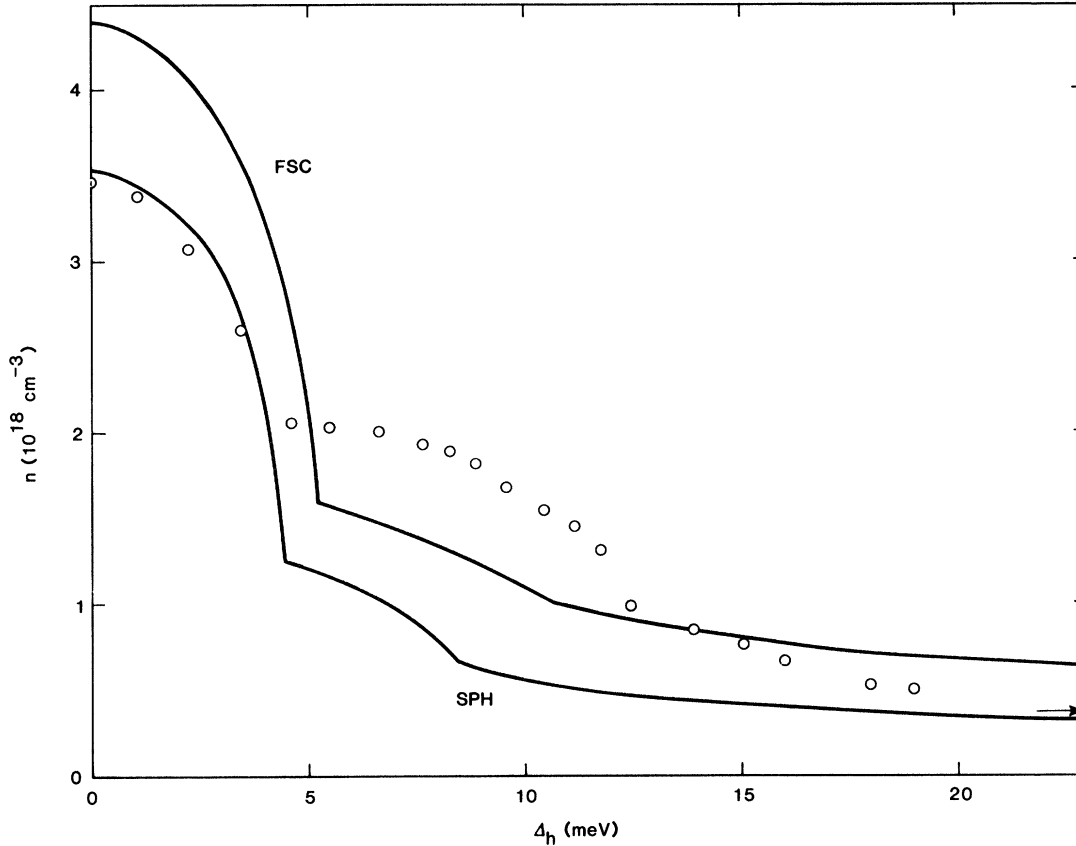


FIG. 15. Density versus valence-band splitting Δ_h . The points are low-stress data from Fig. 14 which have been replotted as a function of Δ_h to compare with theoretical results (solid lines) of Kirczenow and Singwi. The labels SPH (single particle-hole) and FSC (fully self-consistent) denote two different methods for calculating the correlation energy. The arrow indicates our highest stress data corresponding to $\Delta_h = 73$ meV.

level. However, the complicating effect of evaporation was evident in shallow strain wells at low-excitation levels. These decays became more exponential at higher excitation levels. This effect is shown in Fig. 17 for the time decays of EHL in a shallow well with $\sigma = 48$ kg/mm² and $\alpha \simeq 38$ meV/mm². At low excitation the smaller EHL droplets have a larger surface-to-volume ratio and evaporation is more important even though the temperature is very low, $T = 1.4$ K. A similar surface evaporation effect was observed in unstressed Ge when the lattice temperature was raised.^{38,39} For the lower stresses, the time constant of exponential decay at high excitation was taken as the bulk EHL lifetime.

We have fit the EHL decays in Fig. 17 using a solution to a simple set of kinetic equations for a system of EHL and excitons.^{38,39} The rate equation for EHL includes terms for exciton capture

and evaporation from the surface of a droplet as well as e - h recombination in the bulk. Under the assumption that exciton gas density n_{ex} remains reasonably constant, the decay for a droplet with ν e - h pairs is given by the analytic form

$$\nu(t) = \nu_0 e^{-t/\tau} [1 + \rho(1 - e^{t/3\tau})]^3, \quad (8)$$

where ν_0 is the initial number, τ is the bulk EHL lifetime, and

$$\rho = \frac{\tau(\alpha_e - \beta n_{ex})}{\nu_0^{1/3}} \quad (9)$$

is a dimensionless factor which is a measure of the importance of the surface effect. In this equation, α_e and β are evaporation and capture coefficients, respectively. The functional form of Eq. (8) gave a good fit to the data in Fig. 17. This simple analysis suggests that the droplet size increases rapidly with photoexcitation level.

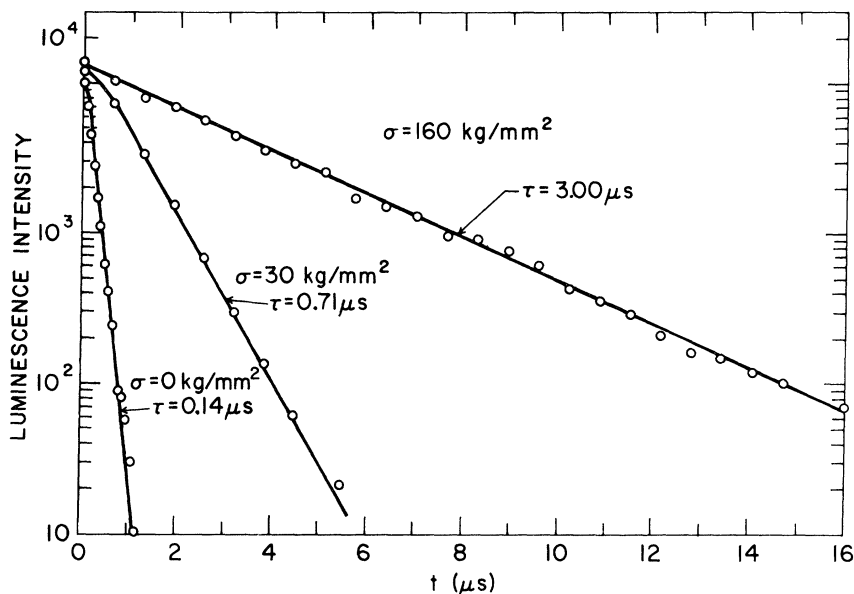


FIG. 16. EHL time decays (points) at zero, intermediate, and very high stresses which correspond to the spectra in Fig. 10. These decays are exponential over a wide range and the lifetime increases sharply with stress. The 20-fold increase in lifetime is directly related to the decrease in density shown in Fig. 14.

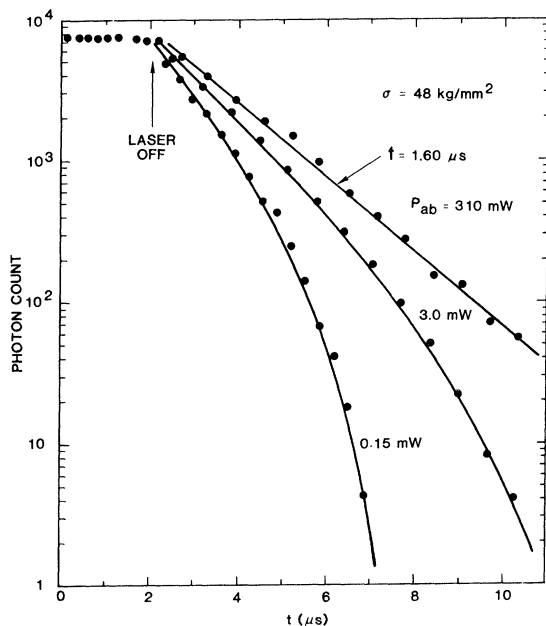


FIG. 17. Experimental time decays (points) of the EHL luminescence, under conditions of moderate stress in a potential well with $\alpha = 38 \text{ meV/mm}^2$, for three different absorbed laser powers P_{ab} . The decays have been normalized to the same initial, steady-state intensity. The arrow indicates the laser off time. The decays at low P_{ab} are nonexponential due to surface evaporation of FE from the EHL. At high levels the decay is exponential and represents the decay of $e-h$ pairs in the bulk of the EHL. The theoretical fits (solid lines) are described in text.

Auger recombination and the enhancement factor

From the above density and lifetime measurements, it is apparent that the Hertzian stress geometry makes it possible to examine the true EHL lifetime over a wide density variation. This data provides the first test of recent theories for the intrinsic EHL recombination process in Si. Equally important, it gives the density variation of the enhancement factor $g_{eh}(0)$, which is proportional to the probability of finding an electron at a hole. The uniform stress measurements with the limitations mentioned above are unable to provide such a test.

A measurement of this type was first carried out for Ge by Chou and Wong,⁴⁰ who used a shallow strain well. They found a sharp increase in the enhancement factor as the density was decreased. A complicating factor in their analysis was the fact that both radiative and nonradiative recombination are important for EHL in Ge. Indeed, the liquid in Ge is about 25% radiatively efficient at zero stress.⁴¹ In the present case the analysis is simpler. The radiative efficiency for Si at liquid He temperatures is estimated to be very low, about 5×10^{-4} .³⁷ This indicates that $e-h$ recombination is strongly dominated by nonradiative processes. In fact, considerable evidence now exists which indicates that the dominant mechanisms involve

Auger recombination. Thus the lifetimes in Si can be more easily analyzed since the radiative mechanisms can be neglected, and an independent measure of the radiative efficiency is not required.

Haug⁴²⁻⁴⁴ recently extended the theory of Auger recombination⁴⁵ to indirect band-gap semiconductors with degenerate e - h concentrations, as applicable to the EHL in Si. He concluded that the principal decay mechanism in Si is a phonon-assisted Auger recombination involving two holes and an electron. In this theory the recombination rate for a single e - h pair has the following density dependence:

$$\frac{1}{\tau} = Cn^2, \quad (10)$$

where C is the Auger coefficient. The exponent 2 follows from a detailed, multiple integral involving degenerate energy distributions. The theoretical value for the Auger coefficient in unstressed Si is $C = 7.2 \times 10^{-31} \text{ cm}^6 \text{ s}^{-1}$.⁴³ It is in reasonable agreement with experimental values determined in previous work^{46,47} and the value determined here, $C = 5.8 \times 10^{-31} \text{ cm}^6 \text{ s}^{-1}$ for unstressed Si. However, a more stringent test of this theory is provided by a density dependence of the EHL lifetime in Si, reported here for the first time. In previous work^{48,49} with doped Si samples at high T where nondegenerate statistics apply, the minority-carrier lifetimes depended quadratically on the majority-carrier concentration at sufficiently high densities, $5 \times 10^{18} - 1 \times 10^{20} \text{ cm}^{-3}$. At lower densities, $10^{18} - 5 \times 10^{18} \text{ cm}^{-3}$, the dependence was less than quadratic. Some of these data seem to show a restored quadratic dependence at even lower density.

In the present work, an exact quadratic dependence is observed at lower densities $(3.5 - 6) \times 10^{17} \text{ cm}^{-3}$. As shown in Fig. 18 the lifetime measured at each stress is plotted against the corresponding density determined from the spectral fits. At low densities $1/\tau \propto n^2$ (dashed line) and the density dependence predicted by Eq. (10) is observed for the EHL in Si. At the lowest density the Auger coefficient is $C = 2.7 \times 10^{-31} \text{ cm}^6 \text{ s}^{-1}$, decreased more than 2 times from the zero-stress value. For densities $6 \times 10^{17} - 3.5 \times 10^{18} \text{ cm}^{-3}$, the measured lifetimes do not lie on the dashed line. This density range corresponds to the range of deviation noted above for carriers in doped Si. This variation from quadratic behavior at these densities may be accounted for by a variation in the enhancement factor $g_{eh}(0)$. Equation (10) may be rewritten

$$\frac{1}{\tau} = C'g_{eh}^2(0)n^2, \quad (11)$$

where C' is a constant independent of density and $g_{eh}(0)$ is displayed explicitly.

The enhancement factor for EHL was calculated by Vashista *et al.*^{13,50} for the configurations Si[6:2] where $g_{eh}(0) = 3.46$, and for Si[2:1] where $g_{eh}(0) = 7.4$. The quantity $g'_{eh}(0) = A/\tau n^2$, where A is a normalization factor, is plotted versus n in Fig. 18. It shows that the enhancement factor decreases with increasing density as previously observed in the case of stressed Ge.⁴⁰ The values are normalized to the zero-stress theoretical value 3.46. Below $n = 6 \times 10^{17} \text{ cm}^{-3}$, which corresponds to $\sigma = 60 \text{ kg/mm}^2$, $g'_{eh}(0)$ stops changing and has a value of 8.0. The ratio of this high-stress value to that for zero stress is 2.31, in close agreement with the result 2.14 computed by Vashista *et al.*¹³

Apparently, the Auger recombination mechanism of Eq. (11), with changes in $g_{eh}(0)$ over a range of values expected from many-body theory, can account for the observed density dependence of the EHL lifetime in Si. However, the theoretical values of $g_{eh}(0)$ increase monotonically as the density is lowered and do not show a leveling off as the data do. This discrepancy is shown in Fig. 19 where the experimental values of $g_{eh}(0)$ (open circles) as well as Vashista's earlier theory⁵⁰ (solid

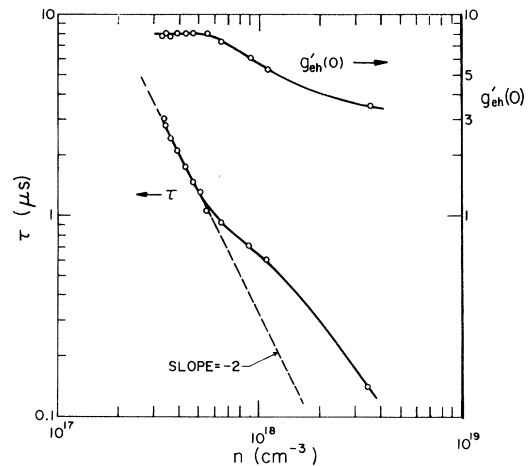


FIG. 18. Lower data points show the EHL lifetime τ versus density n . At low density τ is quadratically dependent on density (dashed line has slope -2) as predicted by Haug (Refs. 42-44). At higher densities there is a deviation from this dependence. It can be accounted for by a changing enhancement factor $g'_{eh}(0)$ (upper data points). The values of $g'_{eh}(0)$ have been normalized to Vashista's zero-stress value of 3.46.

line) for the case $m_e/m_h=1$ have been replotted as a function of mean particle spacing r_s , where $4\pi r_s^3 a_{x0}^3/3=1/n$ with $a_{x0}=49 \text{ \AA}$ the excitonic radius for the simple exciton. The data points are in agreement with theory for the range $r_s=0.82-1.5$. Above $r_s=1.5$ the experimental values approach a constant value in contrast to theory.

However, one should expect the correlation of $e-h$ pairs to reach a limiting value when the "enhanced" density $n_{eh}=g_{eh}(0)n$ approaches the exci-

ton "density" $n_{x0}=|\Psi_{x0}(0)|^2=1/\pi a_o^3$. In Fig. 19 the enhanced density (solid points) has been plotted against r_s . The enhanced density decreased from a zero-stress value of $12.3 \times 10^{18} \text{ cm}^{-3}$ to a high-stress value of $2.5 \times 10^{18} \text{ cm}^{-3}$, which is below the exciton density defined above. In Fig. 19 we have indicated a range (shaded area) for the exciton density. It is bounded below by the density for a simple exciton and above by the density estimated for real excitons with radius

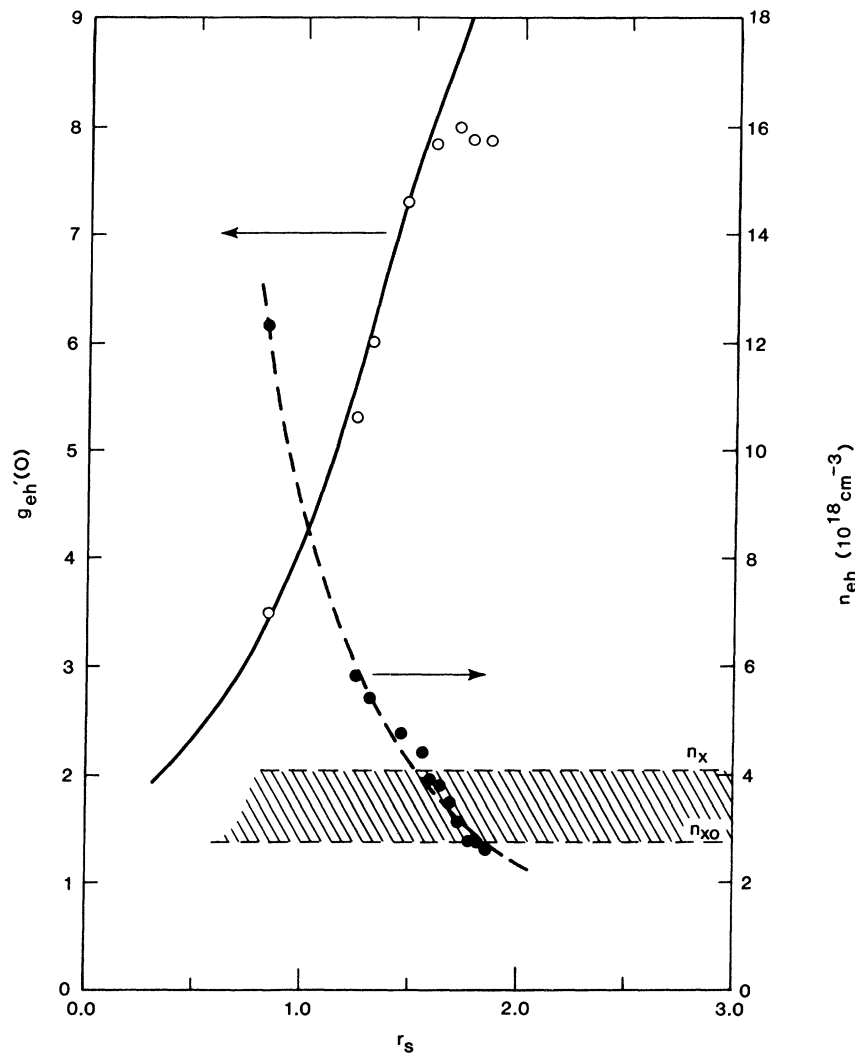


FIG. 19. Enhancement factor $g'_{eh}(0)n$ (left scale) and enhanced density $n_{eh}=g'_{eh}(0)n$ (right scale) versus the particle separation r_s . The open points are data for $g'_{eh}(0)$ determined from Eq. (11) which have been normalized at low r_s to the theory of Vashista *et al.* (Ref. 13) (solid line). There is good agreement between the data and theory for the functional dependence of $g'_{eh}(0)$ on r_s from $r_s=0.8$ to 1.5. Above this range the data for $g'_{eh}(0)$ do not change, in contrast with theory. This discrepancy occurs where the data for the enhanced density (solid points) decreases to the exciton "density" (shaded region). The quantities n_x and n_{x0} are defined in the text.

$$a_x = a_{x0} \left(\frac{E_{x0}}{E_x} \right)^{1/2},$$

where $E_x = 14.7$ meV is the measured exciton binding energy. The enhanced density decreases because the average e - h pair density n decreases more rapidly than the enhancement factor increases. The exciton density remains approximately constant since a_x changes negligibly with stress. From this figure it is clear that the limiting value of $g_{eh}(0)$ occurs near $n_{eh} = n_x$. Beyond $r_s = 1.5$, n_{eh} continues to decrease while $g_{eh}(0)$ remains constant. This simple analysis suggests that the EHL has a strongly metallic character for $n_{eh} > n_x$ and approaches a phase more like an excitonic liquid for $n_{eh} < n_x$. However, this interpretation is difficult to reconcile with existing theories for the gas-to-liquid phase transition.⁵¹ These theories predict that the insulator-to-metal transition should occur simultaneously or before the gas-to-liquid transition. In addition, the emission spectra of an excitonic liquid would have a narrow linewidth. The observed spectra monotonically narrowed (Fig. 10) as the density decreased but remained rather broad, as characteristic of a Fermi liquid. The high-stress liquid phase in Si, with its large electron-hole correlation, clearly presents some interesting questions for future study.

An alternative explanation for the observed values of $g_{eh}(0)$ is that the constant C' in Eq. (11) is stress dependent. Then the quantity plotted in Figs. 18 and 19 represents the stress dependence of the product $\sqrt{C'}g_{eh}(0)$. In this case $g_{eh}(0)$ could still be increasing above $r_x = 1.5$ if $\sqrt{C'}$ was decreasing at the same rate. While this seems unlikely, to examine this possibility one must analyze the stress dependence of the matrix elements occurring in the transition rate for EHL recombination. We have not attempted such an analysis in the present work.

The above measurements of the enhancement factor can be compared to the results of Chou and Wong's measurements of Ge.⁴⁰ There $g_{eh}(0)$ was found to increase rapidly with r_s , even faster than the prediction of Vashista. The enhancement factor increased monotonically from $g_{eh}(0) = 0.67$ at $r_s = 0.60$, to $g_{eh}(0) = 1.86$ at $r_s = 1.32$. As previously mentioned, the analysis for Ge is more complicated because both the radiative and nonradiative rates must be considered. The enhanced density decreased monotonically below n_x at $r_s = 0.8$. The enhancement factor in Ge did not seem to approach a limiting value above this value of r_s , al-

though the high-stress limit was not achieved in those experiments.

V. THERMODYNAMIC PROPERTIES OF EHL

EHL at higher T

In the present section we report data which illustrate the threshold of EHL formation and determine the critical temperature T_c and the binding energy ϕ for EHL in Si in the high-stress limit. Measurements of T_c in the range 26–28 K for unstressed Si have been reported previously.^{52,53} A recent measurement of T_c in unstressed Si by Forchel *et al.*¹⁵ produced a lower value of $T_c = 23$ K. These authors also measured T_c in Si uniformly stressed along the $\langle 100 \rangle$, $\langle 110 \rangle$, and $\langle 111 \rangle$ axes under conditions of intermediate stress. The results were $T_c = 14, 16.4, \text{ and } 16.9$ K, respectively.

To ensure that the photoexcited density was sufficiently large at high T , we used our Ar⁺ laser in multiline mode which resulted in absorbed powers up to 0.5 W. Deleterious crystal heating was avoided by chopping the light with a low duty factor in the range 0.02–0.05. The long laser on-times represent steady-state conditions. Also we optimized the density enhancement afforded by the strain well. The density of an ideal gas in the well is $n = N/V_{\text{eff}}$ where $N = G\tau$, G was given in Eq. (1), and $V_{\text{eff}} = (\pi kT/\alpha)^{3/2}$. From Eq. (5) we see that the well curvature $\alpha \sim R^{-4/3}$ so that $n \sim R^{-2}$ for a given G . Thus very high densities can be achieved with small R . T_c measurements were made with an $R = 0.95$ stresser which corresponds to $\alpha = 550$ meV/mm². For $T = 15$ – 20 K we estimate that we can attain average densities 5×10^{16} – 2×10^{17} cm⁻³, which includes the theoretical critical density.¹³

Using an $\alpha = 90$ meV/mm² strain well, we measured spectra over a wide excitation range to determine the EHL onset. The spectra at low $T = 4.9$ K in Fig. 20 show three distinct peaks, (FE, EM, and EHL), as the absorbed power level P_{ab} increases. At $T = 15$ K in Fig. 21, only FE emission is present at the lowest P_{ab} . At higher pumping a low-energy bump due to EM appears. The EHL grows out of this bump and acquires the distinctive EHL shape which doesn't change with further pumping. At the highest temperatures $T > 20$ K the characteristic EHL emission was not observed. In Fig. 22 the spectra at $T = 22$ K show that the

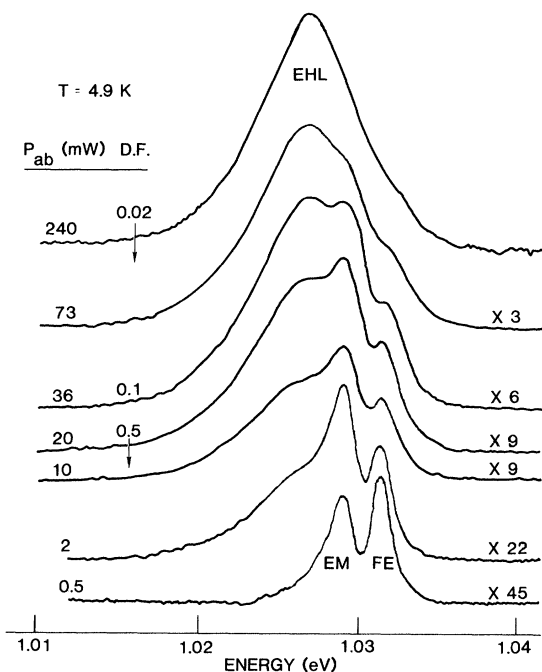


FIG. 20. Evolution of the TO-LO spectrum at $T=4.9$ K with increasing excitation level. Distinct peaks for FE, EM, and EHL are observed. D.F. \equiv laser duty factor.

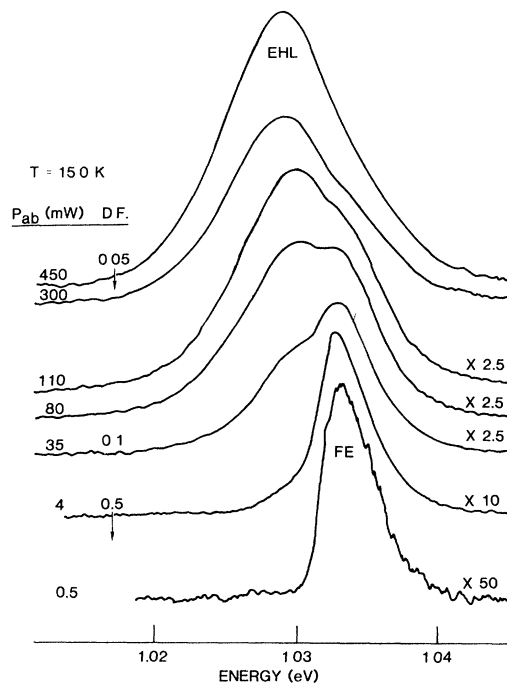


FIG. 21. Evolution of the TO-LO spectrum at $T=15$ K with increasing excitation level. At the highest pump levels, the characteristic line shape of the EHL is observed.

FE peak undergoes a featureless, continuous broadening to lower energy. This broadening is likely due to an electron-hole plasma (EHP) similar to that seen in unstressed Si.^{52,53}

We analyzed the threshold for EHL formation by employing a method similar to that used by Shah *et al.*⁵³ The saturated exciton gas density is determined by the e - h generation rate (calibrated in the manner already discussed) at the onset of EHL, the measured gas volume, and the measured exciton decay time. These decay times increase sharply from 4 to 12 K, similar to that observed in unstressed Si.⁵⁴ The threshold data are shown in Fig. 23.

To measure T_c we pumped a $550\text{-meV}/\text{mm}^2$ well with maximum P_{ab} and low duty factor, and recorded the luminescence spectrum from 1.3 to 40 K. Representative spectra are shown in Fig. 24. To characterize the spectral changes we plotted in Fig. 25 the peak position (B) and the two half-peak height positions (A and C) at each temperature. At higher temperatures $T \approx 20$ K the red edge (C) moved quickly to higher energy away from its low- T position and the renormalized band gap $E'_g(T)$. These data, coupled with that for the EHL

onset, lead us to conclude that the EHL disappears at a critical temperature of $T_c \approx 20$ K.

In Fig. 26 the measured phase diagram (points) is plotted. Also included are the phase diagrams (dashed lines) for unstressed and uniformly stressed Si measured by Kulakovskii *et al.*^{52,55} Note that in contrast to both dashed curves which exhibit a low- T cutoff, the coexistence curve for gas-EHL in the strain well extends to much lower densities. We attribute this to the much longer lifetimes observed for EHL in the strain, as reported in Sec. IV. Also, the phase diagram differs on the liquid side. The characteristic liquid expansion with increasing T was not observed, apparently due to the compressive force of the potential well. This alters the approach to the critical point but should not affect the value of T_c .³⁴

The experimentally determined critical temperature is inside the range of recent T_c estimates for Si[2:1] made by Kelso³⁴ and Liu and Liu^{56,57} using several different models for computing the EHL ground-state energy. These theoretical values ranged from $T_c = 18$ to 24 K. However, several lower values of T_c have been calculated. An earlier calculation of $T_c = 14$ K for stressed Si was

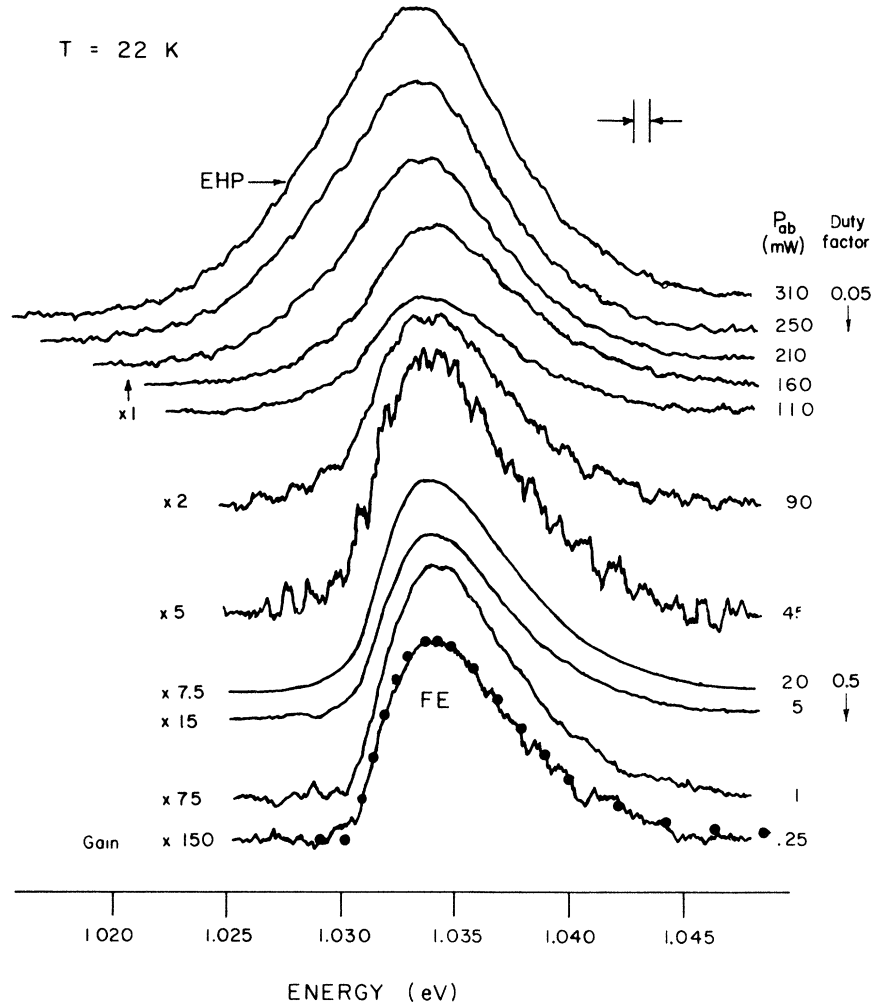


FIG. 22. Evolution of the TO-LO spectrum at $T=22$ K with increasing excitation level. Only a FE peak is present at lower values of P_{ab} . At the highest levels, no EHL line shape is observed. However, a broadening due to electron-hole plasma (EHP) is evident.

made by Vashista *et al.*¹³ Reinecke *et al.*^{58–60} has calculated 14.2 K using a droplet fluctuation model and 17.6 K using a uniform plasma model. Very recently, Forchel *et al.*¹⁵ have experimentally determined $T_c = 14$ K. These values are summarized in Table I.

Having measured both the density and the critical temperature in the high-stress limit, we can investigate one of the general scaling relations for EHL developed by Reinecke and Ying.⁶⁰ The relation is that

$$\frac{\kappa T_c}{n_0^{1/4}} \left(\frac{\kappa}{\mu} \right)^{1/4} \approx \text{const}, \quad (12)$$

where κ is the static dielectric constant and μ is the optically averaged electron-hole reduced mass in units of the bare electron mass. The quantities κ and μ change negligibly from zero to high stresses. Taking $\kappa = 11.4$ (Ref. 61), $\mu = 0.123m_0$, $T_c = 27$ K (Ref. 53), and $n_0 = 3.5 \times 10^{18} \text{ cm}^{-3}$, the quantity in Eq. (12) assumes the values $2.22 \times 10^{-2} \text{ K cm}^{3/4}$ for unstressed Si[6:2]. For the high-stress limit Si[2:1] using $T_c = 20$ K and $n_0 = 3.5 \times 10^{17} \text{ cm}^{-3}$ the value becomes $2.91 \times 10^{-2} \text{ K cm}^{3/4}$, a 30% increase over the stressed value. However, this comparison is made between data corresponding to two different excitation conditions.

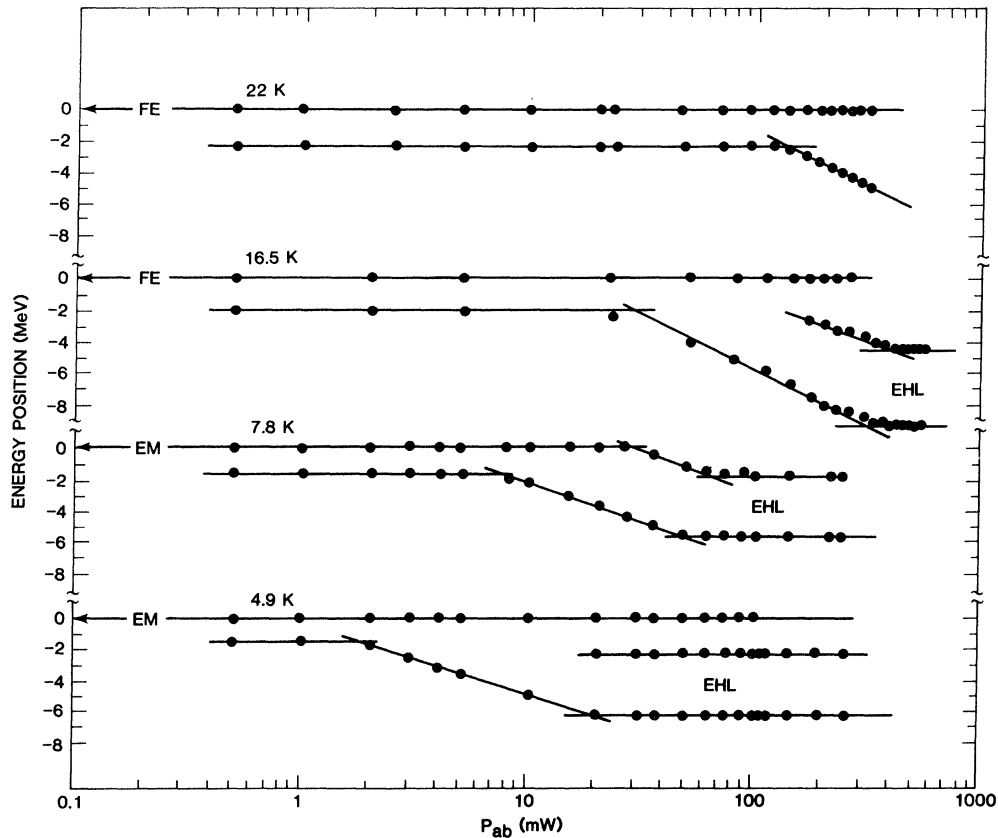


FIG. 23. Plot of lowest energy peak and its low-energy half maximum. This figure shows the production of EHL for $T \lesssim 20$ K. The two lower plots start at low P_{ab} with the EM energy positions while the higher two plots start at low P_{ab} with the FE energy positions.

Binding energy

As anticipated by the later theories for EHL ground-state properties, we find the EHL in Si at high stress to be stable with respect to FE. At $\sigma = 163 \text{ kg/mm}^2$ we measured the EHL binding energy $\phi = 1 \text{ meV}$. This value was obtained by subtracting the spectral position of the EHL Fermi level from the FE zero position. The Fermi level was directly determined from the low- T EHL line fit. Owing to the high gaseous compression affected by the strain well (with $\sigma = 163 \text{ kg/mm}^2$), separate emission from Fe was not observed at low T even at the lowest excitation levels. Consequently, the FE zero position was determined from a high- T FE line fit. Then, the low- T zero position was obtained by accounting for the accurately known T -shift of the band edge.⁶²

In addition to the high-stress measurement stated above, we measured ϕ at intermediate stresses

($\sigma \approx 50$ and 90 kg/mm^2) using the same method. In each case $\phi \approx 1 \text{ meV}$, the same value obtained for high stress. Previous measurements of the binding energy at intermediate stresses are summarized in Table I along with theoretical values for ϕ in the infinite-stress limit. Some authors have reported excellent agreement with the theoretical result of $\phi = 1.9 \text{ eV}$ by Vashista *et al.*¹³ In the present work and one previous paper¹⁴ the agreement is less than satisfactory.

Because the binding energy is small, its measurement should be sensitive to the exact method of fitting both the EHL and FE line shapes. It has been reported that the EHL fitting function which incorporates lifetime broadening produces a larger (15%) binding energy for the zero-stress spectrum. However, as we have pointed out, this theory for the line shape predicts that lifetime broadening effects, should diminish as the e - h pair density decreases with stress.

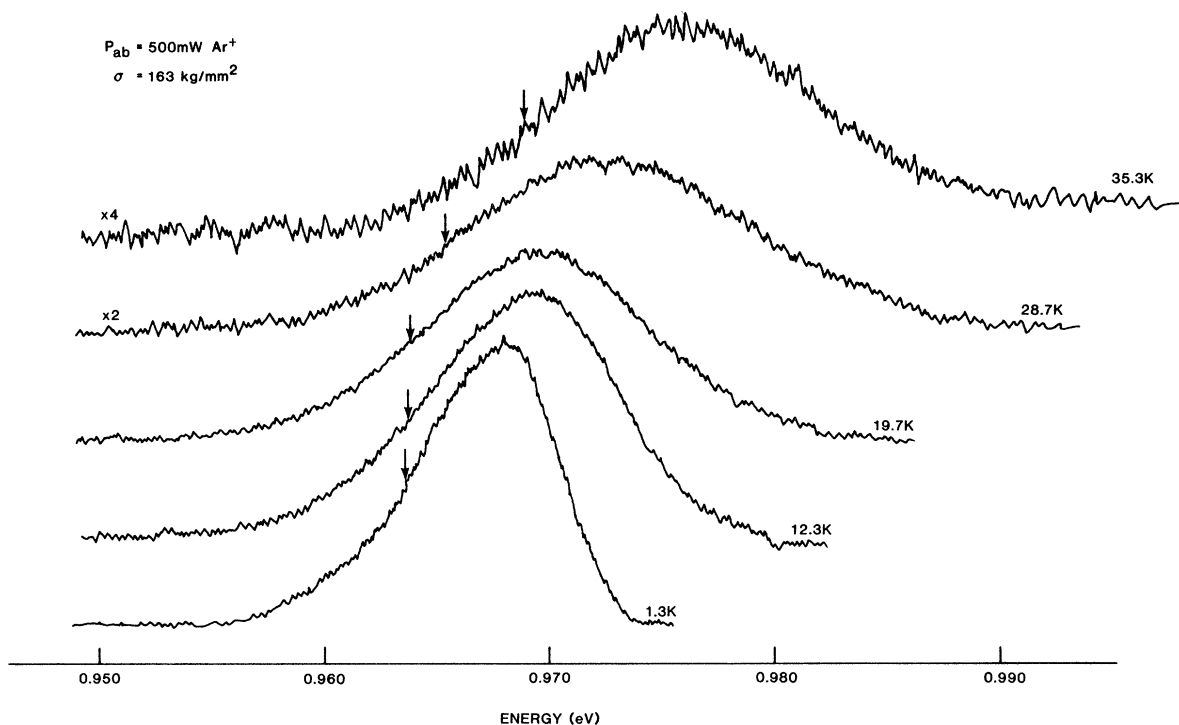


FIG. 24. Photoluminescence spectrum over a wide T range under conditions of very high e - h pair density. The argon laser was operated in the multiline mode to produce high peak power but was modulated with a low duty factor, D.F.=0.03, to avoid crystal heating. The carriers were confined in a highly compressive potential well ($\alpha=550$ meV/mm²) with high stress. The low- T spectrum corresponds to the EHL line shape while the high- T spectrum is predominantly due to the gas phase. At intermediate T both liquid and gaseous phases contribute to produce a broad, unresolved line shape. We determine a critical temperature for EHL from the shift in the low-energy half height position (arrow) as shown in Fig. 25.

A thermodynamic value for ϕ can be determined from the gas-liquid phase boundary shown in Fig. 26. Due primarily to the long EHL lifetime, the form of this coexistence curve is in agreement with that predicted by equilibrium thermodynamics. This curve determines an activation energy of 1.4 meV. However, one must be cautious in making a direct association of this values with ϕ because the onset of the liquid occurs in gas containing *both* EM and FE. Nevertheless, both thermodynamic and spectroscopic ϕ measurements are consistent and allow us to conclude that the EHL is definitely bound in the high-stress limit.

VI. SPATIAL PROPERTIES

As we have reported in Sec. III, the density of the strain-confined EHL in the high-stress limit is $n=3.5 \times 10^{17} \text{ cm}^{-3}$. It is interesting to compare this spectroscopic density with the average e - h pair

density $n_{av}=G\tau/V$, determined by measuring the total generation rate G , the lifetime τ , and the EHL volume V . The quantity G is related to the incident power as shown in Eq. (1). The volume is determined by measuring the full width at half maximum Δ of the spatial profile. For a spherical volume $V=(\sqrt{2}/3)\pi\Delta^3$. For a shallow potential well with $\alpha=38 \text{ meV/mm}^2$, we find $n_{av}=2.8 \times 10^{15} \text{ cm}^{-3}$. This value is only 1% of the spectroscopic density. Obviously, this shallow well does not contain a large single EHL drop as was observed in the case of Ge.¹⁷⁻¹⁹ This particular well must contain a distribution of widely spaced EHL droplets. Since the strain gradient will force droplets together, some repulsive force between droplets is required to explain the large spatial distribution. One possibility is the "phonon wind" force proposed by Keldysh.⁶³

The flux of phonons emitted from a droplet can be absorbed and scattered by another droplet. Accordingly, the droplets are *mutually repelled* with a

TABLE I. Comparison of theory and experiment for ground-state parameters of EHL with $\langle 100 \rangle$ stress.

Experiment	n_0 (10^{17} cm $^{-3}$)	ϵ_{Fe} (meV)	ϵ_{Fn} (meV)	T_c (K)	ϕ (meV)	$g_{eh}(0)$	n_c (10^{17} cm $^{-3}$)	C (10^{-31} cm 6 s $^{-1}$)	τ (μ s)	σ (kg/mm 2)
Present work	3.5	3.6	7.1	20	1-1.4	8.0	2.5	2.7	3.0	163
Wagner and Sauer (Ref. 14)	6.0	5.1	11.0		0.3					28
Forchel <i>et al.</i> (Ref. 15)	4.8			14.0	2.1		1.8			69
Kulakovskii <i>et al.</i> (Refs. 6, 12, and 55)	4.8	4.4	9.3	14	2					48
Theory										
Vashista <i>et al.</i> (Ref. 13)	4.5	4.2	9.1	14.3	1.9	7.4	1.7			∞
Kirzenow and Singwi (Ref. 33)	2.8-5.1	3.1-4.5	6.3-9.3		0.13-2.7					$\Delta_h = 50$ meV
Reinecke <i>et al.</i> (Refs. 15 and 69) droplet fluctuations	4.5			14.2	1.9		1.4			∞
uniform plasma				17.6			0.78			∞
Kelso (Ref. 34)	4.2-4.7	4.0-4.3	8.7-9.5	18.3-24.4	1.2-1.9		0.48-0.78			∞
Haug (Ref. 44) (unstressed)								7.2		0

force that falls off with $1/r^2$ where r is the inter-droplet separation. The phonons are created by e - h recombination and thermalization of energetic Auger particles. As we have shown in our kinetics data, Auger recombination is dominant in Si. It is also possible that, depending upon the carrier thermalization times, the repulsive force could be transmitted directly by Auger particles emitted from the droplets. In the discussion that follows we explicitly consider a phonon "wind" to account for the observed repulsive force. However, the results of this discussion are equally valid for any repulsive force that follows a $1/r^2$ law.

In analogy with electrostatic forces, the droplets can be assigned a "charge" density ρ according to the magnitude of the momentum transferred to a drop per unit time. Keldysh has proposed that

$$\rho^2 = \begin{cases} \frac{a^{ab}}{4\pi} \frac{n_0 E_g}{\tau_0} \frac{d^2 m^2}{\hbar^3 \rho_c s} |\vec{k}|, & |\vec{k}| < 2k_F \\ \frac{a^{sc}}{4\pi} \frac{n_0 E_g}{\tau_0} \left[\frac{d^2 m^2}{\hbar^3 \rho_c} \right]^2 \frac{|\vec{k}|^4}{\omega_k^3}, & |\vec{k}| \gg 2k_F \end{cases} \quad (13)$$

$$(14)$$

where n_0 is the e - h pair density in the droplet, τ_0 the liquid lifetime, E_g the energy gap, d is the effective deformation potential, m is an effective mass, ρ_c is the atomic density of the crystal, s is the speed of sound, and a^{ab} and a^{sc} are the absorption cross sections for absorption and scattering of phonons. A cutoff in absorption occurs at twice the Fermi momentum $2k_F$.

Keldysh's result predicts that above a critical droplet radius the phonon wind would fissure the droplet, countering the droplet surface tension which holds it together. He estimated the droplet radius would be limited to approximately $1 \mu\text{m}$ in unstressed Si. In stressed Si the density is reduced and the lifetime increases. Also, the cutoff $2k_F$ decreases which lessens the absorption cross section of a droplet. This would increase the critical size of the droplets and thus increase the filling factor. The added compressional force of the strain gradient in a potential well would further increase the filling factor.

We can predict the density distribution for droplets and the filling factor by balancing the restoring force of the strain well which acts on a droplet against the phonon force. The net phonon wind force on a droplet is determined by applying Gauss's law to a spherically symmetric average density distribution given by

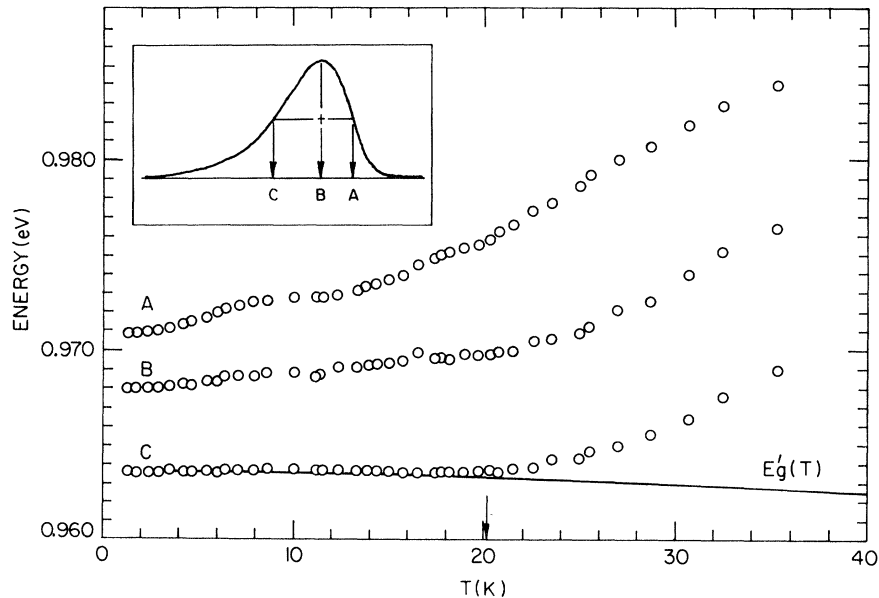


FIG. 25. Spectral positions of *A* (blue edge), *B* (peak), and *C* (red edge) points of the EHL line shape defined in the inset, versus temperature. The critical temperature (marked by arrow) is determined when the red edge starts to deviate from the solid line labeled $E_g'(T)$ which is the energy band gap normalized to the red edge position at low temperature. The stress here is 163 kg/mm^2 which is well into the high-stress limit.

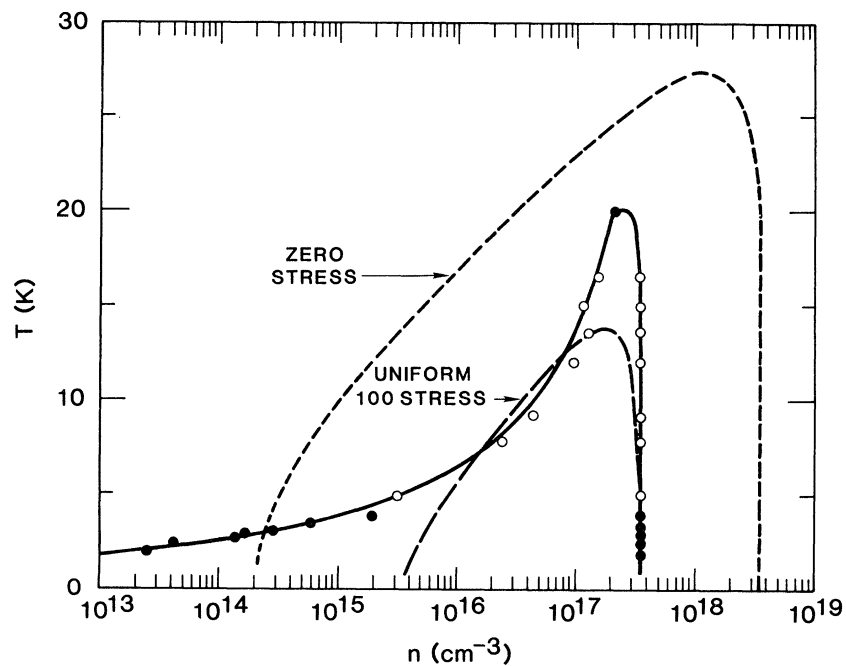


FIG. 26. Measured phase diagram (points) for excitonic gas-EHL in the strain well. The solid point near the determined critical point ($T_c = 20 \text{ K}$, $n_c = 2.5 \times 10^{17} \text{ cm}^{-3}$) corresponds to $\sigma = 163 \text{ kg/mm}^2$. The open points correspond to $\sigma = 90 \text{ kg/mm}^2$. To observe the low- T EHL onset (solid points at low T) it was necessary to use a shallow well which corresponds to $\sigma = 50 \text{ kg/mm}^2$. For comparison the data of Kulakovskii *et al.* (Refs. 52 and 55) for unstressed and $\langle 100 \rangle$ uniformly stressed crystals are indicated.

$$n(r) = \frac{4}{3} \pi r_0^3 n_d(r) n_0 = f(r) n_0, \quad (15)$$

where $n_d(r)$ is the distribution of droplets, r_0 is the droplet radius, and f is the filling factor equal to 1 for a contiguous volume of EHL. In this simple model we neglect diffusion of droplets and attenuation of the phonon wind due to absorption. The opposing forces of the wind and the well balance with a constant average distribution

$$n_{av} = \frac{3}{2\pi} \frac{\alpha n_0^2}{\rho^2}. \quad (16)$$

As expected the average density increases with the degree of curvature α and decreases with the strength of the phonon wind. This result allows us to deduce a value for ρ^2 from the measured quantities n_{av} , n_0 , and α . For the typical experimental values quoted at the beginning of this section we find that $\rho^2 = 8 \times 10^{19} \text{ eV/cm}^5$. This value has the same order of magnitude as the result estimated by Keldysh.

Since Eq. (16) is independent of the total number of e - h pairs, it predicts that the total volume of the cloud of EHL droplets will increase linearly with the excitation level G . However, measurements of the spatial extent Δ show that this is not the case. The volume expands more slowly, approximately as $V \propto G^{1/2}$. The peak height I of the luminescence profile increases linearly with G . Thus the average density, which is proportional to I/Δ^2 , increases with excitation level. This dependence of n_{av} on G for a well with $\alpha = 90 \text{ meV/mm}^2$ is shown in Fig. 27. The average density increases

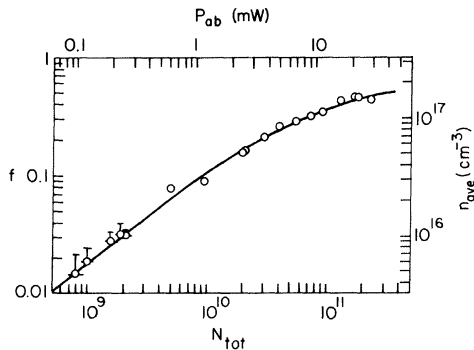


FIG. 27. Average density n_{av} or filling factor f versus absorbed power P_{ab} or total number of e - h pairs N_{tot} . The average density increases by a factor of 30 approaching the liquid density of $3.5 \times 10^{17} \text{ cm}^{-3}$ where $f=1$. The error bars at lower density indicate the uncertainty due to spatial resolution.

about 30 times when the excitation is increased by 100. The filling factor increases from 0.01 at low levels to a value that asymptotically approaches 1. It is very probable that average pair density is approaching that of a large single drop. This is to be contrasted with measurements of the spatial profile of the EHL cloud in unstressed Si (Ref. 64) and Ge (Refs. 65 and 66) where $n_{av} = \text{const}$ and $f \approx 0.01$ over a wide range of carrier generation rate.

We conclude that, at moderate pumping conditions, the average carrier density in the strain well is 2 orders less than the EHL density. The large disparity can be accounted for by a repulsive phonon wind force. However the wind apparently becomes much weaker at high densities, perhaps due to a macroscopic phonon screening due to absorption of the phonons by droplets.

VII. DISCUSSION AND SUMMARY

We have presented a variety of data for the EHL in Si over a wide range of $\langle 100 \rangle$ stress by using both uniform- and Hertzian stress configurations. We have carefully analyzed the experimental Hertzian stress distribution and found it to exhibit the analytical features of the ideal Hertzian distribution. By using this knowledge to manipulate the stress distribution, we were able to obtain certain experimental advantages over uniform-stress geometries. In particular, very high stresses, e - h pair confinement with spatial control, and density enhancement permitted new experimental investigations of the EHL. At lower stresses, we produced corresponding uniform and Hertzian stresses which give identical EHL emission line shapes. Using both geometries, we determined the EHL density and lifetime from line-shape data over stresses $\sigma = 0 - 163 \text{ kg/mm}^2$. These data showed no evidence of inhomogeneous strain broadening. Thus the Hertzian stressing technique can produce very high effective uniform stress for studying the degenerate EHL in Si.

Our analysis of the EHL line shape demonstrates the importance of including the proper stress-dependent density of valence-band states for σ less than about 100 kg/mm^2 . Any analysis that does not include the valence-band nonparabolicity present at lower stresses, will result in densities that are appreciably smaller than the actual values. For example, in a previous density measurement by

the present authors⁷ at $\sigma \approx 50 \text{ kg/mm}^2$ the line shape was fit to a density of $3.2 \times 10^{17} \text{ cm}^{-3}$ using the infinite stress band structure. In the present analysis, that density is corrected to $5.1 \times 10^{17} \text{ cm}^{-3}$, an increase of 60%. Even though our present analysis tends to increase the spectroscopic density, the narrow line shape at $\sigma = 163 \text{ kg/mm}^2$ gave $n = 3.5 \times 10^{17} \text{ cm}^{-3}$ which is the lowest experimental value for Si (by $\sim 30\%$) reported to date.

Even at this low e - h pair density, the observed line shape displays a long, low-energy tail, a fact that is in apparent discrepancy with the previously forwarded lifetime broadening ideas. An understanding of this effect may require a more detailed model which incorporates kinetic processes that affect the radiative recombination events.

The strain well was particularly valuable for studying the intrinsic recombination time of the EHL. In contrast to previous uniform-stress experiments, we were able to measure the bulk EHL lifetime over a tenfold reduction in e - h pair density. At low density, the lifetime shows an exact quadratic dependence on density as predicted by theories for Auger recombination. At higher densities this relation is modified due to changes in the e - h correlation. We observed that the e - h correlation is a rapidly increasing function of particle separation as predicted by theory. A marked discrepancy between experiment and theory occurs when the enhanced e - h density is equal to the "exciton density." This suggests that the low-density phase of EHL has a nature similar to an exciton liquid.

When the EHL stability is reduced by crystal strain, surface evaporation of e - h pairs from the droplets is expected to greatly increase and can be an important decay mechanism even at low T . The boiloff effect may be greater in Si than Ge because of the large surface-to-volume rates of small EHD. If the EHL is strain confined, the effects of surface evaporation are not usually present because backflow of FE into droplets is provided. However, under special conditions, nonexponential decays were observed. The form of these decays is consistent with exciton-EHL rate equations, including surface evaporation.

Our data suggests that the average droplet size increases with the stress gradient (and stress) and excitation level. The question of droplet size versus stress is a complicated one because several physical parameters enter. In Keldysh's theory,⁶³ the droplet size is limited by internal phonon wind pressure. The maximum drop size is

$$r_0 = \left(\frac{15 S}{2\pi \rho^2} \right)^{1/3}, \quad (17)$$

where S is the surface tension. Kalia and Vashista⁶⁷ have calculated that S in Si decreases eight times from zero to infinite $\langle 100 \rangle$ stress. Countering this reduction in S , ρ^2 [see Eqs. (13) and (14)] decreases by 200 over the same range due to the changes in liquid density and lifetime. These simple arguments predict a threefold increase in the $r_0 \approx 1 \mu\text{m}$ drop size originally predicted by Keldysh for unstressed Si.

Previously, it was shown that the EHL in Ge forms a single, macroscopic drop ($\sim 1 \text{ mm}$) when strain confined.^{18,19} This is not true in the present case. Our spatial studies show that the strain-confined EHL in Si normally exists as a cloud of smaller droplets. As we have mentioned, the droplet size probably increases with the strain gradient. The droplet size also increases with increasing excitation level, while the cloud extent expands slowly. The net effect is to increase the average e - h pair density such that the EHL volume approaches that of a single, large drop. It would be of considerable interest to perform Rayleigh light-scattering experiments on the strain-confined liquid to determine the droplet size as a function of exciton density, temperature, and strain-well restoring force. Previous attempts to observe Rayleigh scattering from EHD in unstressed Si failed, presumably due to the small droplet radius. However, the larger droplets predicted for the strain well should be amenable to this type of measurement.

The critical temperature measured here $T_c = 20 \text{ K}$ is higher than the value $T_c = 14 \text{ K}$ reported for uniformly stressed Si.¹⁵ There are several possible explanations for this discrepancy. The $T_c = 14 \text{ K}$ result may be a lower threshold temperature due to insufficient e - h density. In our experiments the e - h density is greatly enhanced by the strain gradient. In addition, the effective EHL lifetime is more than $10\times$ longer in the strain well. This longer lifetime is highly desirable for the determination of the liquid-gas coexistence curve. Kulakovskii *et al.*⁵⁵ have found that in uniformly stressed Si the phase boundary occurs at higher densities than predicted by equilibrium thermodynamics. The difference is most pronounced at low T . It is likely that the short effective lifetime and surface tension modify the observed phase boundary as in the case of unstressed Si. In contrast, we find for the longer-lived, strain confined EHL an equilibrium-like coexistence curve which extends to very low

density and temperature.

An alternate explanation for the different T_c 's would be that the critical point is modified by EHL compression in the strain gradient. However, no effects of compression in the low-temperature EHL line shape were detected. This result is in contrast to the large compression observed for strain-confined EHL in Ge (Refs. 21 and 22) where the liquid formed a single large drop. These interesting compression effects are apparently much more difficult to produce. We believe that this is because (a) the compressibility of EHL in Si is expected to be much lower than for Ge, and (b) liquid compression should not be significant when the EHL is in the form of a cloud of droplets as in Si.

Since the compressibility of the EHL increases with temperature we cannot completely rule out an effect of compression in the determination of T_c . However very similar results were obtained for widely differing potential-well steepness, $\alpha=90$ and 550 meV/mm^2 , indicating an insensitivity to strain gradient. In addition, Kelso³⁴ has pointed out that the presence of the strain well should not alter T_c . Above T_c only the gas-phase exists, no matter how great the pressure.

Our experiments have demonstrated the highly desirable features of a parabolic potential well in characterizing the excitonic gas-liquid system. Of particular importance in future work is the nearly classical liquid-gas boundary, which displays none of the deviations present for short-lived EHD in unstressed or uniformly stressed samples. The strain-confined system shows promise for detailed studies of the phase boundary near the critical point.

ACKNOWLEDGMENTS

We gratefully acknowledge E. E. Haller for providing us with the high-purity Si sample and Ge detector crystal. M. V. Klein loaned us the high-sensitivity phototube. We acknowledge useful discussions with S. M. Kelso. This work was supported in part by the National Science Foundation under a Materials Research Laboratory Grant No. NSF-DMR077-23999 and a Cottrell Research grant. During the writing of this paper, P. L. Gourley was supported by Sandia National Laboratories under Contract No. DE-AC04-76-DP00789, a U. S. Department of Energy facility.

APPENDIX A

EHL line-shape fitting procedure

The EHL pair density in unstressed crystals was first determined from the spectroscopic line shape by Kaminskii and Pokrovskii.²⁷ By including the stress dependence of the electron and hole densities of states, the same method may be used to determine the EHL density in stressed crystals. This modified method is similar to that used by Kelso.³⁴

Stress-dependent densities of states

The stress-dependent densities of states may be determined from the energy spectra for electrons and holes in the stressed crystal.^{68,69} For parabolic energy dispersion, the electron density of states D_e is simply determined by a sum over the stress-split conduction bands. In the case of a $\langle 100 \rangle$ stress

$$D_e(\epsilon_e, \sigma) = \frac{2m_{de}^{3/2}}{\sqrt{2}\pi^2\hbar^3} [d_1\epsilon_e^{1/2} + d_2(\epsilon_e - \Delta_e)^{1/2} \times u(\epsilon_e - \Delta_e)] \quad (\text{A1})$$

where the electron energy ϵ_e is measured from the bottom of the lowest conduction-band minima and $d_1=2$ and $d_2=4$ are degeneracies of the lower and upper bands, respectively. The quantity $\Delta_e(\sigma)$ is the stress-induced energy splitting of these conduction bands and $u(\epsilon)$ is the unit step function. The m_{de} is the density-of-states mass.

The more complicated expressions for the energy E_h of the light and heavy holes require the stress-dependent density of hole states D_h to be determined by numerical integration.

$$D_h(\epsilon_h, \sigma) = \frac{2}{(2\pi)^3} \times \sum_n d_n \int_S d\Omega \frac{k^2(\epsilon_h, \theta, \phi)}{|\nabla_{\vec{k}} E_h^{(n)}(\vec{k}, \sigma)|_{k=k(\epsilon_h, \theta, \phi)}} \quad (\text{A2})$$

Here, the sum is over the stress-split light- and heavy-hole bands. These bands exhibit nonparabolicity and change significantly with stress. The integral is over the surface S where the hole energy ϵ_h is constant. The magnitude of the hole wave vector k varies over this surface. The band degeneracies (excluding spin) are $d_n=1$. The function D_h , for various stresses from zero stress to the

high-stress limit, is shown in Fig. 4.

Knowing the densities of states, the electron (hole) density $n_{e(h)}$ can be determined by

$$n_{e(h)} = \int d\epsilon_{e(h)} D_{e(h)}(\epsilon_{e(h)}) f_{e(h)}(\epsilon_{e(h)}). \quad (\text{A3})$$

This evaluation for the holes must be done numerically. At $T=0$ K the electron density can be evaluated explicitly

$$n_e = \frac{d_1}{3\pi^2} \left[\frac{2m_{de}}{\hbar^2} \right]^{3/2} \epsilon_{Fe}^{3/2} + \frac{d_2}{3\pi^2} \left[\frac{2m_{de}}{\hbar^2} \right]^{3/2} (\epsilon_{Fe} - \Delta_e)^{3/2}. \quad (\text{A4})$$

Line shape and fitting procedure

The stress-dependent densities of electron and hole states were then used in the usual convolution integral. The resulting EHL line shape contained four parameters: the stress σ , the electron and hole Fermi energies ϵ_{Fe} and ϵ_{Fh} , and the temperature T :

$$I_{\text{EHL}} = I_{\text{EHL}}(h\nu'; \sigma, \epsilon_{Fe}, \epsilon_{Fh}, T). \quad (\text{A5})$$

The stress was determined by comparing the energy position of the EHL or FE peak with that in uniform-stress experiments. The linewidth of the fitting function increases with the Fermi energies. Thus, the object of the fitting procedure was to determine those Fermi energies which duplicated the experimental linewidth. The measured lattice temperature was used in all fits.

An initial guess was made for the hole Fermi energy. Then the hole density n_h was determined by numerical integration using Eq. (A3) for holes. Charge neutrality requires that $n_e = n_h$. This allowed the corresponding ϵ_{Fe} to be found by inverting Eq. (A4) numerically. Once the Fermi energies were known, the line shape was generated. The spectral FWHM of this theoretical line shape was determined and compared with experimental linewidth. The "best fit" was defined as the theoretical line shape with the same FWHM as the experimental line shape. Since there is no simple relationship between the FWHM and the density, a table of corresponding values of FWHM and ϵ_{Fh} was formed. Then, the experimental density and Fermi energies were found by interpolation, using the experimental FWHM. Three of these best-fit line shapes, at zero, intermediate, and high stress, are shown in Fig. 10.

*Present address: Sandia National Laboratories, Albuquerque, NM 87185.

¹See the review by J. C. Hensel, T. G. Phillips, T. M. Rice, and G. A. Thomas, *Solid State Physics*, edited by H. Ehrenreich, F. Seitz, and D. Turnbull (Academic, New York, 1977), Vol. 32.

²G. A. Thomas and V. B. Timofeev, in *Handbook on Semiconductors*, Vol. 2 of *Optical Properties of Solids*, edited by M. Balkanski (North-Holland, Amsterdam, 1980), Chap. 2.

³L. V. Keldysh, *Proceedings of the Ninth International Conference on the Physics of Semiconductors, Leningrad, 1968* (Nauka, Leningrad, 1968), p. 1303.

⁴B. M. Ashkinadze, I. P. Kretsu, A. A. Patrin, and I. K. Yaroshetskii, *Fiz. Tekh. Poluprovodn.* **4**, 2206 (1970) [*Sov. Phys.—Semicond.* **4**, 1897 (1971)].

⁵C. Benoît à la Guillaume and M. Voos, *Phys. Rev. B* **5**, 3079 (1972).

⁶V. D. Kulakovskii and V. B. Timofeev, *Zh. Eksp. Teor. Fiz. Pis'ma Red.* **25**, 487 (1977) [*JETP Lett.* **25**, 458 (1977)].

⁷P. L. Gourley and J. P. Wolfe, *Phys. Rev. Lett.* **40**, 526 (1978).

⁸M. L. W. Thewalt and J. A. Rostworowski, *Solid State Commun.* **25**, 991 (1978).

⁹V. D. Kulakovskii, V. B. Timofeev, and V. M. Edelstein, *Zh. Eksp. Teor. Fiz.* **74**, 372 (1978); in *Proceedings of the 14th International Conference on the Physics of Semiconductors, Edinburgh, 1978*, edited by B. L. H. Wilson (Institute of Physics, Bristol, 1978).

¹⁰P. L. Gourley and J. P. Wolfe, *Phys. Rev. B* **20**, 3319 (1979).

¹¹W. F. Brinkman and T. M. Rice, *Phys. Rev. B* **7**, 1508 (1973).

¹²V. D. Kulakovskii, V. B. Timofeev, and V. M. E'del'shtein, *Zh. Eksp. Teor. Fiz.* **74**, 372 (1978) [*Sov. Phys.—JETP* **47**, 193 (1978)].

¹³P. Vashista, Shashikala G. Das, and K. S. Singwi, *Phys. Rev. Lett.* **33**, 911 (1974).

¹⁴J. Wagner and R. Sauer, *Phys. Status Solidi B* **94**, 69 (1979).

¹⁵A. Forchel, B. Lawrich, G. Moersch, W. Schmid, and T. L. Reinecke, *Phys. Rev. Lett.* **46**, 678 (1981).

¹⁶M. Tajima, *Appl. Phys. Lett.* **32**, 719 (1978).

¹⁷R. S. Markiewicz, J. P. Wolfe, and C. D. Jeffries, *Phys. Rev. Lett.* **32**, 1357 (1974).

¹⁸J. P. Wolfe, R. S. Markiewicz, C. Kittel, and C. D. Jeffries, *Phys. Rev. Lett.* **34**, 275 (1975).

¹⁹J. P. Wolfe, W. L. Hansen, E. E. Haller, R. S. Markiewicz, C. Kittel, and C. D. Jeffries, *Phys. Rev. Lett.*

- 34, 1292 (1975).
- ²⁰J. P. Wolfe, R. S. Markiewicz, S. M. Kelso, J. E. Furneaux, and C. D. Jeffries, *Phys. Rev. B* **18**, 1479 (1978).
- ²¹S. M. Kelso and J. E. Furneaux, *Solid-State Electron.* **21**, 1377 (1978).
- ²²S. M. Kelso, in *Proceedings of the 14th International Conference on the Physics of Semiconductors, Edinburgh, 1978*, edited by B. L. H. Wilson (Institute of Physics, Bristol, 1978), p. 363.
- ²³R. S. Markiewicz and S. M. Kelso, *Solid State Commun.* **25**, 275 (1978).
- ²⁴R. S. Markiewicz, J. P. Wolfe, and C. D. Jeffries, *Phys. Rev. B* **15**, (1977).
- ²⁵H. Hertz, *J. Math (Crelles)* **92**, 156 (1881).
- ²⁶S. Timoshenko and J. N. Goodier, *Theory of Elasticity*, 2nd ed. (McGraw-Hill, New York, 1951), Chap. 13.
- ²⁷A. S. Kaminskii and Y. E. Pokrovskii, *Zh. Eksp. Teor. Fiz. Pis'ma Red.* **11**, 381 (1970) [*JETP Lett.* **11**, 255 (1970)].
- ²⁸P. T. Landsberg, *Phys. Status Solidi* **15**, 623 (1966).
- ²⁹R. W. Martin and H. L. Stormer, *Solid State Commun.* **22**, 523 (1977).
- ³⁰J. P. Wolfe and P. L. Gourley, in *Proceedings of the 14th International Conference on the Physics of Semiconductors, Edinburgh, 1978*, edited by B. L. H. Wilson (Institute of Physics, Bristol, 1978).
- ³¹R. B. Hammond, T. C. McGill, and J. W. Mayer, *Phys. Rev. B* **13**, 3566 (1976).
- ³²J. A. Rostworowski, *Solid State Commun.* **28**, 919 (1978).
- ³³G. Kirczenow and K. S. Singwi, *Phys. Rev. B* **21**, 3597 (1980).
- ³⁴S. M. Kelso, Ph.D. thesis, University of California, Berkeley (1979) (unpublished).
- ³⁵W. Schmid, *Solid State Commun.* **19**, 347 (1976).
- ³⁶W. Schmid, *Phys. Status Solidi B* **94**, 413 (1979).
- ³⁷J. D. Cuthbert, *Phys. Rev. B* **1**, 1552 (1970).
- ³⁸R. M. Westervelt, T. K. Lo, J. L. Staehli, and C. D. Jeffries, *Phys. Rev. Lett.* **32**, 1051 (1974).
- ³⁹J. C. Hensel, T. G. Phillips, and T. M. Rice, *Phys. Rev. Lett.* **30**, 227 (1973).
- ⁴⁰H. H. Chou and G. K. Wong, *Phys. Rev. Lett.* **41**, 1677 (1978).
- ⁴¹K. Betzler, B. G. Zhurkin, and A. L. Karuzskii, *Solid State Commun.* **17**, 577 (1975).
- ⁴²A. Haug, *Solid State Commun.* **22**, 537 (1977).
- ⁴³A. Haug, *Solid State Commun.* **25**, 477 (1978).
- ⁴⁴A. Haug, *Solid-State Electron.* **21**, 1281 (1978).
- ⁴⁵See also W. Lochmann, *Phys. Status Solidi A* **45**, 423 (1978).
- ⁴⁶W. Schmid, *Solid-State Electron.* **21**, 1285 (1978).
- ⁴⁷M. H. Pilkuhn, *J. Lumin.* **18/19**, 81 (1979).
- ⁴⁸J. D. Beck and R. Conradt, *Solid State Commun.* **13**, 93 (1973).
- ⁴⁹J. Dziejwior and W. Schmid, *Appl. Phys. Lett.* **31**, 346 (1977).
- ⁵⁰P. Vashista, P. Bhattacharyya, and K. S. Singwi, *Phys. Rev. B* **10**, 5108 (1974).
- ⁵¹E. Hanamura and H. Haug, *Phys. Rep.* **C33**, (1977).
- ⁵²A. F. Dite, V. D. Kulakovskii, and V. B. Timofeev, *Zh. Eksp. Teor. Fiz.* **72**, 1156 (1977) [*Sov. Phys.—JETP* **45**, 604 (1977)].
- ⁵³J. Shah, M. Combescot, and A. H. Dayem, *Phys. Rev. Lett.* **38**, 1497 (1977).
- ⁵⁴R. B. Hammond and R. N. Silver, *Appl. Phys. Lett.* **36**, 68 (1980).
- ⁵⁵V. D. Kulakovskii, I. V. Kihuskin, and V. B. Timofeev, *Proceedings of the 15th International Conference on the Physics of Semiconductors, Kyoto, 1980* [*J. Phys. Soc. Jpn.* **49**, Suppl. A (1980), p. 527].
- ⁵⁶L. Liu and Lu Sun Liu, *Solid State Commun.* **27**, 801 (1978).
- ⁵⁷L. Liu, *Solid State Commun.* **25**, 805 (1978).
- ⁵⁸M. Lega, T. L. Reinecke, and S. C. Ying, *Bull. Am. Phys. Soc.* **23**, 422 (1978).
- ⁵⁹T. L. Reinecke, M. C. Lega, and S. C. Ying, *Phys. Rev. B* **20**, 1562 (1979).
- ⁶⁰T. L. Reinecke and S. C. Ying, *Phys. Rev. Lett.* **43**, 1054 (1979).
- ⁶¹R. A. Faulkner, *Phys. Rev.* **184**, 713 (1969).
- ⁶²Y. P. Varshni, *Physica (Utrecht)* **34**, 149 (1967).
- ⁶³L. V. Keldysh, *Zh. Eksp. Teor. Fiz. Pis'ma Red.* **23**, 100 (1976) [*JETP Lett.* **23**, 86 (1976)].
- ⁶⁴M. Tamor and J. P. Wolfe, *Phys. Rev. B* **21**, 739 (1980).
- ⁶⁵M. Greenstein and J. P. Wolfe, *Phys. Rev. Lett.* **41**, 715 (1978).
- ⁶⁶M. Greenstein and J. P. Wolfe, *Solid State Commun.* **33**, 309 (1980).
- ⁶⁷R. K. Kalia and P. Vashista, *Phys. Rev. B* **17**, 2655 (1978).
- ⁶⁸G. L. Bir and G. E. Pikus, in *Symmetry and Strain-Induced Effects in Semiconductors*, translated by P. Shelnitz, edited by D. Louvish (Keter, Jerusalem, 1974).
- ⁶⁹G. E. Pikus and G. L. Bir, *Fiz. Tverd. Tela (Leningrad)* **1**, 1642 (1959).